Gravitational Collapse of a Magnetized Star

Diplomarbeit

von

Niels Oppermann

betreut von

Prof. Dr. K. D. Kokkotas

Eberhard Karls Universität Tübingen
Fakultät für Mathematik und Physik
Institut für Astronomie und Astrophysik
Abteilung Theoretische Astrophysik

Oktober 2009

Erklärung gemäß § 18 (7) der Diplomprüfungsordnung

Hiermit erkläre ich, dass ich diese Arbeit selbständig verfasst und keine anderen als die angegebenden Quellen und Hilfsmittel benutzt habe.

Tübingen, 29. Okt. 2009

Niels Oppermann

Zusammenfassung

In dieser Arbeit wird der Kollaps eines Sterns mittels numerischer Simulationsrechnungen untersucht. Dabei wird die dynamische Entwicklung elektromagnetischer Felder miteinbezogen. Zu diesem Zweck wird ein numerischer Code entwickelt, der in der Lage ist, den sphärisch-symmetrischen Kollaps einer Kugel zu beschreiben, die als ideale Flüssigkeit mit einer polytropischen Zustandsgleichung beschrieben wird. Die dafür verwendeten Gleichungen sind voll-relativistisch und der Code kann die Entstehung eines Ereignishorizontes während des Kollaps behandeln. Ein magnetisches Feld durchsetzt den Stern anfänglich und erstreckt sich in Form eines einfachen Dipol-Feldes in den Außenraum. Die zeitliche Entwicklung dieses Feldes wird im Innenraum unter der Annahme idealer Magnetohydrodynamik analytisch durchgeführt und im Außenraum numerisch. Dabei werden die Rückwirkungen des elektromagnetischen Feldes auf die Dynamik der Flüssigkeit und das Gravitationsfeld nicht berücksichtigt. Um die Gültigkeit der mit dem numerischen Code erzielten Ergebnisse zu überprüfen werden diverse Vergleiche mit analytischen Resultaten und früheren numerischen Studien gezogen. Dann werden die Eigenschaften einer beim Kollaps entstandenen elektromagnetischen Welle untersucht.

Insbesondere wird der Fall berücksichtigt, in dem der stellare Kollaps zur Entstehung eines Neutronensterns führt. Auch in diesem Fall werden elektromagnetische Felder zeitentwickelt. Um einen Neutronenstern zu erhalten wird eine hybridartige Zustandsgleichung angenommen, welche zwei verschiedene Adiabatenindices für hohe und niedrige Massendichten enthält. Mit diesem Modell wird der Zusammenhang zwischen den Eigenschaften des Sternes und denen der emittierten elektromagnetischen Welle untersucht. Als Ergebnis wird eine Möglichkeit aufgezeigt, die Eigenschaften des Sternes durch die Beobachtung der elektromagnetischen Strahlung zu bestimmen.

Abstract

In this work, we examine stellar collapse with a dynamical evolution of electromagnetic fields by means of numerical simulation. To this end, a numerical code is developed that can follow the spherical collapse of a perfect fluid ball described by a polytropic equation of state. The equations used are fully relativistic and the code can handle the formation of an event horizon during the collapse. A magnetic field initially threads the star and extends into the exterior in the form of a purely dipole field. This field is evolved analytically in the stellar interior with the ideal MHD approximation and numerically in the exterior. The backreactions of the electromagnetic fields onto the fluid dynamics and the gravitational field are neglected. In order to check our new code, many comparisons to analytic results and earlier numerical studies are made. Then, the properties of a resulting electromagnetic wave are studied.

Especially, the case of the formation of a neutron star after the stellar collapse is considered, also including a magnetic field. To produce a neutron star, a hybrid equation of state is adopted, which contains two different adiabatic indices for high and low densities. With this model, we examine the relation between the stellar properties and the emitted electromagnetic wave. As a result, we find the possibility to determine the stellar properties via the observation of electromagnetic waves.

Acknowledgements

While working on this diploma thesis, I have benefited from the excellent advice given by both **Dr. Hajime Sotani** and **Prof. Dr. Kostas Kokkotas**, as well as from the good atmosphere within the Theoretical Astrophysics group at the University of Tübingen, for which all its members are to be credited.

Furthermore, I was supported financially by the SFB/TR7 on Gravitational Wave Astronomy.

Contents

1 Introduction **8**
1.1 Physical Relevance 8
1.2 Previous Work 9
1.3 Outline 10

2 Conventions **11**

3 General Relativistic MHD in (3+1)-Formulation **12**
3.1 (3+1)-decomposition of the metric 12
3.2 The ADM Formalism 12
3.3 The MHD-Equations 15
3.3.1 Equations of Relativistic Hydrodynamics 15
3.3.2 Maxwell Equations 16
3.3.3 The Ideal MHD Approximation 17
3.3.4 Equations of Relativistic MHD 18

4 Hydrodynamic Collapse **19**
4.1 Equations in Hernandez-Misner coordinates 19
4.2 Numerical Implementation 25
4.3 Testbed Calculations 28
4.3.1 Oppenheimer-Snyder collapse 28
4.3.2 Tolman-Bondi Collapse 31
4.4 Collapse of a Polytropic Star 37
4.5 Further Numerical Tests 39
4.5.1 Influence of Initial Hypersurface 39
4.5.2 Finding the Onset of Instability 40
4.5.3 Oscillation Frequencies 40
4.5.4 Long-term Stability 41
4.5.5 Determining the Order of Accuracy 42

5 Evolution of Electromagnetic Fields **44**
5.1 Evolution Equations 44
5.1.1 Interior 44
5.1.2 Exterior 45
5.2 Boundary Conditions 47
5.3 Initial Field Configuration 50
5.3.1 Interior 50
5.3.2 Exterior 51
5.4 Numerical Implementation 52
5.5 Calculated Magnetic Fields 55
5.6 Tests of the Numerical Scheme 57
5.6.1 Wavelength of the Radiation 57
5.6.2 Late-Time Behavior 57
5.6.3 Energy Conservation 64

6 Collapse to a Neutron Star **69**
6.1 Equation of State 69
6.2 Numerical Results 69
6.2.1 Electromagnetic Radiation 70

7 Concluding Remarks **75**

A Finite Difference Equations for the Hydrodynamic Evolution Scheme **77**

1 Introduction

This work deals with the numerical simulation of a collapsing star, including electromagnetic fields both in the stellar interior and exterior. The star could be very compact and therefore the gravitational field becomes very strong. In fact, a black hole may be formed during the final stages of the collapse. Therefore the scenario calls for a fully general relativistic description.

1.1 Physical Relevance

There are a number of different astrophysical scenarios containing a collapsing object, most of them being somehow related to the end of a star's life (cf. e.g. [8]).

The core of an actively burning star is supported either by thermal pressure provided by nuclear fusion reactions or by electron degeneracy pressure or by a combination of both. At some point, fuel for the nuclear reactions will become scarce and the thermal pressure reduced. Alternatively or in addition, the core may grow to exceed its Chandrasekhar mass which is the maximum mass that can be supported by the degeneracy pressure. Either way it will become radially instable and the collapse can occur.

Stars with masses larger than approximately 40 to 50 solar masses are expected to collapse directly to a black hole, more or less as described in chapters 4 and 5. Less massive stars will end their lives in a supernova explosion, i.e. their cores will collapse until they form a neutron star, similar to the scenario in chapter 6, where only the core is modelled. This termination of the collapse sends a shockwave through the outer layers of the star which triggers the explosion. After that, the gravitational binding energy of the newly formed neutron star is transferred by some not very well understood mechanism to the stellar envelope which is then expulsed. However, only stars in a mass range between eight to ten solar masses and 20 to 25 solar masses are expected to produce a supernova explosion with a neutron star as a remnant. At the end of a supernova explosion of a star with a mass between 20 to 25 solar masses and 40 to 50 solar masses, enough material will fall back onto the nascent neutron star to force it to collapse to a black hole. Stars with masses of less than eight solar masses on the other hand are expected to contract until they form a white dwarf supported by electron degeneracy pressure ([8]).

If such a white dwarf is part of a binary system it may accrete matter from its companion, thus it would ultimately exceed its Chandrasekhar mass and collapse. In this accretion induced collapse, rotation – probably differential – is likely to play a very prominent role. Therefore the assumptions made in this work, among them spherical symmetry, are not well adjusted to this scenario.

Other more exotic collapse scenarios include the collapse of a supermassive star ($M \geq 10^6 M_\odot$) to a supermassive black hole or the collapse of a star of the first generation in the early universe (cf. [8]). Another scenario that may lead to collapse is the merger of two neutron stars. The combined mass of the two stars may be higher than the critical mass leading the resulting object

to collapse eventually. However, in this case rotation is again likely to be an important part of the dynamics so the applicability of the results presented here is limited.

Numerical simulations can be of help in addressing a wide range of questions dealing with the dynamics of a core-collapse supernova. For example, modelling the collapsing core will give predictions on whether the supernova remnant will be a black hole or a neutron star. The magnetic field of the core might influence the outcome via magnetic stresses in the matter acting as an additional stabilising source of pressure.

A core-collapse supernova is also a very promising candidate as a source of gravitational waves. Since the object in question is very compact and highly dynamical, the expected amplitudes are of an interesting order of magnitude also for future detection. Not only during collapse will gravitational waves be generated, but also afterwards. During the bounce, oscillations in the supernova-core may be excited, making the supernova remnant a possible continuous source of gravitational waves.

Detailed numerical studies of core-collapse including microphysical aspects, such as the energy loss due to neutrino emission, can be of help in addressing the question of the explosion mechanism.

Although the present work does not take into account any layers of matter outside of the collapsing sphere, nor any complicated microphysics or realistic equations of state, it may yet give a reasonable account of the events taking place in the interior of a core-collapse supernova, given that the rotation is sufficiently slow to justify the approximation of spherical symmetry.

1.2 Previous Work

Work in the field of numerical modellations of gravitational collapse started in the 1960s when May and White published two papers ([14],[15]) introducing a numerial scheme to solve the coupled equations of hydrodynamics and General Relativity in spherical symmetry.

Since then, progress was made largely along two lines: On the one side, the scenario was generalized to less symmetric settings, keeping the fully relativistic formulation of the equations but using oversimplified models to describe the matter and the hydrodynamics. On the other side, people managed to introduce detailed microphysics including realistic equations of state, radiation and neutrino transport etc. but handling the gravitational field as Newtonian. (Cf. [7] for an extensive review of the work along both of these lines.)

A large portion of the numerical work on gravitational collapse is carried out with the goal of modelling a source for gravitational waves. Reference [8] is a review of this field (cf. also [18]).

Our work is based in large parts on the numerical evolution scheme proposed by Baumgarte, Shapiro, and Teukolsky in reference [4], where the equations used by May and White are changed by introducing a null coordinate (chapter 4). A scenario similar to the one presented in chapter 5 was already

studied by Baumgarte and Shapiro in reference [2], where the magnetic field is evolved on the analytically determined background of Oppenheimer-Snyder collapse. Some of their formalism is taken over and their results serve for comparison.

1.3 Outline

The set of equations that needs to be evolved brings together the Einstein field equations of General Relativity, the conservation of energy-momentum and baryon number of hydrodynamics, and the Maxwell equations of electrodynamics. Chapter 3 is a brief review of the derivation of these equations in a general form.

In chapter 4, the scenario is specified to an isolated, perfectly spherical ball of matter outside of which there is nothing but pure vacuum. The matter is assumed to be a perfect fluid described by a polytropic equation of state. A coordinate system that is suitable for the numerical evolution is chosen and the equations derived in chapter 3 are cast in these coordinates. In the case of a star which is described by a single polytropic equation of state, the collapse invariably leads to the formation of a black hole. A number of numerical tests proving the accuracy of the code are performed.

The magnetic field is added to this scenario in chapter 5. It is assumed that this field initially is a pure dipole field. Furthermore, the stellar matter is assumed to be perfectly conducting, which is a reasonable approximation for highly ionized hot plasmas. For simplicity, the backreaction of the electromagnetic fields onto the dynamics of the matter and onto the gravitational field are disregarded. In this way, the rest of the simulation stays spherically symmetric and can be used unchanged as a background on which to evolve the electromagnetic fields.

In chapter 6, the equation of state is changed in a way that it becomes stiffer for densities above a certain critical density. Thus, the collapse of an initially less dense object can be obstructed such that it does not lead to the formation of a black hole but to a neutron-star-like object.

2 Conventions

Throughout this work, the sign convention is used that the flat Minkowski metric is

$$[\eta_{\mu\nu}] = \mathrm{diag}\,(-1, 1, 1, 1)\,, \tag{2.1}$$

geometrized units are used such that

$$G = 1 = c \tag{2.2}$$

and greek indices are used to denote spacetime components (0,1,2,3), while latin indices denote spatial components (1,2,3). An indexed quantity enclosed by squared brackets represents the whole object, not just one component, as e.g. $[\eta_{\mu\nu}]$ above.

3 General Relativistic MHD in (3+1)-Formulation

The problem of magnetohydrodynamics in general is to evolve a configuration defined by the mass density, pressure, velocity, energy density and electromagnetic fields given at an initial moment into the future.

In General Relativity this problem is altered on the one hand by the necessity to define additionally the geometry of space at an initial moment and on the other hand by the ambiguity of the term "initial moment". When considering a global inertial system with a definite coordinate system containing a timelike coordinate t, one can define the initial time e.g. by $t_{\text{init}} = 0$. This coordinate system will however be by no means unique in general curved spacetimes, assuming there still exists a global coordinate system with a timelike coordinate. Setting the timelike coordinate to zero in two different coordinate systems will generally define two different hypersurfaces and thus give two different meanings to the term "initial moment".

The idea of the (3+1)-formulation of general relativistic magnetohydrodynamics is to *choose* a family of spacelike hypersurfaces, thus defining surfaces of simultaneity, and to break down the covariantly four-dimensional equations into parts along these hypersurfaces and parts orthogonal to them.

3.1 (3+1)-decomposition of the metric

In order to achieve a formulation of the Einstein equations in space-time-splitting, it is necessary to split the metric into a part describing the intrinsic geometry of each three dimensional hypersurface and a part describing the way in which these slices are oriented with respect to each other. Using coordinates (t, x^i, x^j, x^k) which are adapted to the choice of hypersurfaces, i.e. each hypersurface corresponds to $t = const.$, one can define a spacelike metric $\gamma_{ij}(t, x^i, x^j, x^k)$ on each spacelike slice.

The information on the geometry along the 4-vector normal to the spacelike slices can be encoded in the lapse function and the shift vector. That is, the lapse function α determines by which amount proper time changes from one slice to the next and the shift vector β^i determines the shift in coordinates between two neighboring slices. This leads to the formula

$$ds^2 = -\alpha^2 dt^2 + \gamma_{ij}(dx^i + \beta^i dt)(dx^j + \beta^j dt) \tag{3.1}$$

for the 4-dimensional line element (cf. [3]).

3.2 The ADM Formalism

Arnowitt, Deser and Misner (hereafter ADM) [1] used a variational approach to derive the (3+1)-formulation of the Einstein field equations (cf. also [17]).

The standard action associated with geometrodynamics is

$$S = \int d^4x\mathcal{L} = \frac{1}{16\pi}\int d^4x(-g)^{1/2}R, \tag{3.2}$$

where g is the determinant of the 4-metric and R is the Ricci curvature scalar associated with the spacetime geometry.

ADM introduce, in addition to the quantities discussed above, the momenta conjugate π_{ij} of the metric field, which can be written in terms of the extrinsic curvature tensor

$$K_{ij} = \frac{1}{2\alpha}\left(\beta_{i|j} + \beta_{j|i} - \gamma_{ij,t}\right) \tag{3.3}$$

as

$$\pi^{ij} = -\gamma^{1/2}\left(K^{ij} - \gamma^{ij}K\right). \tag{3.4}$$

Here, a vertical line $|$ denotes a covariant derivative with respect to the spatial 3-metric, $K = K^i_i$ is the trace of the extrinsic curvature tensor and γ is the determinant of the 3-metric.

In terms of these quantities, the Lagrangian from equation (3.2) is

$$\mathcal{L} = -\gamma_{ij}\pi^{ij}{}_{,t} - \alpha\mathcal{H} - \beta_i\mathcal{H}^i - 2\left(\pi^{ij}\beta_j - \frac{1}{2}\pi^k_k\beta^i + \gamma^{1/2}\alpha^{|i}\right)_{,i}, \tag{3.5}$$

where

$$\mathcal{H} = \gamma^{-1/2}\left(\pi^{ij}\pi_{ij} - \frac{1}{2}\left(\pi^k_k\right)^2\right) - \gamma^{1/2}R, \tag{3.6}$$

$$\mathcal{H}^i = -2\pi^{ij}{}_{|j}. \tag{3.7}$$

To this, a Lagrangian desccribing the contributions of any additional fields has to be added. The term in brackets in equation (3.5) will cancel once the integral $\int d^4x\mathcal{L}$ is computed, thus making the effective Lagrangian

$$\mathcal{L} = -\gamma_{ij}\pi^{ij}{}_{,t} - \alpha\mathcal{H} - \beta_i\mathcal{H}^i + \mathcal{L}_{\text{fields}}, \tag{3.8}$$

where e.g.

$$\mathcal{L}_{\text{em}} = -\frac{1}{16\pi}F^{\mu\nu}F_{\mu\nu} \tag{3.9}$$

is the Lagrangian representing electromagnetic fields (cf. [20]).

The energy-momentum tensor associated with the fields is then defined by

$$T_{\mu\nu} = -2\frac{\delta L_{\text{fields}}}{\delta g^{\mu\nu}} + g_{\mu\nu}L_{\text{fields}}, \tag{3.10}$$

where

$$L_{\text{fields}} = (-g)^{-1/2}\,\mathcal{L}_{\text{fields}}. \tag{3.11}$$

Variation of the momenta π^{ij} leads to the evolution equation for the 3-metric

$$\gamma_{ij,t} = 2\alpha\gamma^{-1/2}\left(\pi_{ij} - \frac{1}{2}\gamma_{ij}\pi^k_k\right) + \beta_{i|j} + \beta_{j|i}, \tag{3.12}$$

whereas variation of the 3-metric γ_{ij} leads to the evolution equation for the momenta

$$\begin{aligned}\pi^{ij}{}_{,t} &= -\alpha\gamma^{1/2}\left(R^{ij}-\frac{1}{2}\gamma^{ij}R\right)+\frac{1}{2}\alpha\gamma^{-1/2}\gamma^{ij}\left(\pi^{kl}\pi_{kl}-\frac{1}{2}\left(\pi^{k}_{k}\right)^{2}\right)\\ &\quad -2\alpha\gamma^{-1/2}\left(\pi^{ik}\pi^{j}_{k}-\frac{1}{2}\pi^{ij}\pi^{k}_{k}\right)+\gamma^{1/2}\left(\beta^{|ij}-\gamma^{ij}\beta^{|k}_{|k}\right)+\left(\pi^{ij}\beta^{k}\right)_{|k}\\ &\quad -\beta^{i}_{|k}\pi^{kj}-\beta^{j}_{|k}\pi^{ki}-8\pi\alpha\left(S^{ij}-\frac{1}{2}\gamma^{ij}\left(S-\rho\right)\right).\end{aligned} \tag{3.13}$$

Varying the lapse function α and the shift vector components β^i leads to the Hamiltonian constraint

$$\mathcal{H}=16\pi\rho\gamma^{1/2} \tag{3.14}$$

and the momentum constraint

$$\mathcal{H}^{i}=16\pi S^{i}\gamma^{1/2}. \tag{3.15}$$

Here, $S=S^i_i$ and the source terms are given by the projections of the energy-momentum tensor onto the spatial slices and onto the orthogonal direction respectively:

$$\rho=n_\mu n_\nu T^{\mu\nu}, \tag{3.16}$$

$$S_i=-\gamma_{i\mu}n_\nu T^{\mu\nu}, \tag{3.17}$$

$$S_{ij}=\gamma_{i\mu}\gamma_{j\nu}T^{\mu\nu}, \tag{3.18}$$

where $[n_\mu]=(-\alpha,0,0,0)$ is the unit normal vector to the slices.

Inserting the definition of the momenta (3.4) and equations (3.6) and (3.7) into equations (3.12)-(3.15) yields the ADM equations in the following form (cf. [3]):

$$\gamma_{ij,t}=-2\alpha K_{ij}+\beta_{i|j}+\beta_{j|i}, \tag{3.19}$$

$$\begin{aligned}K_{ij,t} &= -\alpha_{|ij}+\alpha\left(R_{ij}-2K_{ik}K^{k}_{j}+KK_{ij}\right)\\ &\quad -8\pi\alpha\left(S_{ij}-\frac{1}{2}\gamma_{ij}\left(S-\rho\right)\right)+\beta^{k}K_{ij,k}+K_{kj}\beta^{k}_{,i}+K_{ik}\beta^{k}_{,j}\end{aligned} \tag{3.20}$$

$$R+K^{2}-K_{ij}K^{ij}=16\pi\rho, \tag{3.21}$$

$$\left(K^{ij}-\gamma^{ij}K\right)_{|j}=8\pi S^{i}. \tag{3.22}$$

Note that equation (3.19) is a reproduction of the definition of the extrinsic curvature (3.3).

3.3 The MHD-Equations

In addition to the Einstein field equations in the previous section, the equations governing the dynamics of a magnetized fluid are needed. These are contained in the conservation of energy-momentum

$$T^{\mu\nu}{}_{;\nu} = 0 \tag{3.23}$$

and the conservation of baryons

$$(\rho_0 u^\mu)_{;\mu} = 0, \tag{3.24}$$

as well as the Maxwell equations

$$F^{\mu\nu}{}_{;\nu} = 4\pi \mathcal{J}^\mu \tag{3.25}$$

and

$$F_{[\mu\nu;\rho]} = 0. \tag{3.26}$$

Here, ρ_0 is the fluid's rest mass density as measured by a comoving observer, u^μ is the fluid's 4-velocity, $F^{\mu\nu}$ is the Faraday tensor, $\mathcal{J}^\mu$ is the electromagnetic 4-current density and $T^{\mu\nu}$ is the energy-momentum tensor of the fluid and the electromagnetic fields.

3.3.1 Equations of Relativistic Hydrodynamics

Assuming that no electromagnetic fields are present and the fluid can be modelled as a perfect fluid, the energy-momentum tensor becomes

$$T^{\mu\nu} = \rho_0 h u^\mu u^\nu + P g^{\mu\nu}, \tag{3.27}$$

where P is the isotropic pressure, ϵ the specific internal energy density and

$$h = 1 + \epsilon + P/\rho_0 \tag{3.28}$$

the specific enthalpy.

In casting the equations in (3+1)-form, it is convenient to use the following quantities first defined by Wilson in 1972 [25] (cf. also [3]):

$$v^j = \frac{u^j}{u^t} \tag{3.29}$$

as a spatial velocity,

$$D = \rho_0 W \tag{3.30}$$

as a measure of rest mass density,

$$E = \rho_0 \epsilon W \tag{3.31}$$

as a measure of energy density and

$$S_\mu = \rho_0 h W u_\mu \tag{3.32}$$

as a measure of momentum, where $W = \alpha u^t$.

Thus, the continuity equation (3.24) becomes

$$\left(\gamma^{1/2} D\right)_{,t} + \left(\gamma^{1/2} D v^j\right)_{,j} = 0. \tag{3.33}$$

The energy equation

$$\left(\gamma^{1/2} E\right)_{,t} + \left(\gamma^{1/2} E v^j\right)_{,j} = -P \left(\left(\gamma^{1/2} W\right)_{,t} + \left(\gamma^{1/2} W v^j\right)_{,j}\right) \tag{3.34}$$

is acquired by contracting equation (3.23) with u_μ, while the spatial components of equation (3.23) yield the Euler equation (cf. [3])

$$\left(\gamma^{1/2} S_i\right)_{,t} + \left(\gamma^{1/2} S_i v^j\right)_{,j} = -\alpha \gamma^{1/2} \left(P_{,i} + \frac{S_\mu S_\nu}{2\alpha S^t} g^{\mu\nu}{}_{,i}\right). \tag{3.35}$$

These equations are written in a form that contains only partial derivatives which are split explicitly between space and time and the variables have a clear physical meaning.

3.3.2 Maxwell Equations

Decomposing the Faraday tensor into the spatial electric field E^μ and the spatial magnetic field B^μ according to

$$F^{\mu\nu} = n^\mu E^\nu - n^\nu E^\mu + \epsilon^{\mu\nu\rho} B_\rho, \tag{3.36}$$

where $\epsilon^{\mu\nu\rho} = \epsilon^{\mu\nu\rho\sigma} n_\sigma$ and decomposing the electromagnetic 4-current density into the electric charge density ρ_{el} and the spatial electric current density J^μ according to

$$\mathcal{J}^\mu = n^\mu \rho_{\mathrm{el}} + J^\mu \tag{3.37}$$

leads to the Maxwell equations in (3+1) form (cf. [3],[5]): Contracting equation (3.25) with n_μ yields

$$E^i_{|i} = 4\pi \rho_{\mathrm{el}}, \tag{3.38}$$

whereas the projection onto the spatial hypersurfaces, i.e. multiplication with $\gamma^i_\mu = g^i_\mu + n^i n_\mu$, gives (cf. [5])

$$E^i_{,t} = \epsilon^{ijk} \left(\alpha B_k\right)_{|j} - 4\pi\alpha J^i + \alpha K E^i + \beta^j E^i_{,j} - \beta^i_{,j} E^j. \tag{3.39}$$

Similarly, the projection of equation (3.26) onto the direction orthogonal to the spacelike slices yields

$$B^i_{|i} = 0, \tag{3.40}$$

while its projection onto the spacelike slices gives

$$B^i_{,t} = -\epsilon^{ijk} \left(\alpha E_k\right)_{|j} + \alpha K B^i + \beta^j B^i_{,j} - \beta^i_{,j} B^j. \tag{3.41}$$

Now introducing a 4-vector potential $\mathcal{A}_\mu$, which consists of the electrostatic potential Φ and the spatial magnetic vector potential A_μ,

$$\mathcal{A}_\mu = \Phi n_\mu + A_\mu, \tag{3.42}$$

the Faraday tensor can be written as

$$F_{\mu\nu} = \mathcal{A}_{\nu,\mu} - \mathcal{A}_{\mu,\nu}. \tag{3.43}$$

Equating equation (3.36) and equation (3.43) and contracting with $\epsilon^{\mu\nu\rho}$ yields (cf. [3])

$$B^i = \epsilon^{ijk} A_{k,j}. \tag{3.44}$$

Following [3], one can rewrite the Maxwell equations completely in terms of the electric field E^i and the magnetic potential A^i. The evolution equations (3.39) and (3.41) become

$$\begin{aligned} E^i_{,t} &= \left(\alpha A^{j|i}\right)_{|j} - \left(\alpha A^{i|j}\right)_{|j} - 4\pi\alpha J^i + \alpha K E^i + \beta^j E^i_{,j} - \beta^i_{,j} E^j \\ &= \gamma^{-1/2}\left(\alpha\gamma^{1/2}\left(\gamma^{ik}\gamma^{jl} - \gamma^{il}\gamma^{jk}\right) A_{l,k}\right)_{,j} \\ &\quad -4\pi\alpha J^i + \alpha K E^i + \beta^j E^i_{,j} - \beta^i_{,j} E^j \end{aligned} \tag{3.45}$$

and

$$A_{i,t} = -\alpha E_i - (\alpha\Phi)_{,i} + \beta^j E_{i,j} + \beta^j_{,i} E_j. \tag{3.46}$$

3.3.3 The Ideal MHD Approximation

Ohm's law can be written in the form (cf. [3])

$$\mathcal{J}_\mu - \tilde{\rho}_{\text{el}} u_\mu = \sigma F_{\mu\nu} u^\nu, \tag{3.47}$$

where σ is the electrical conductivity and $\tilde{\rho}_{\text{el}} = -\mathcal{J}^\nu u_\nu$. Contracting equation (3.47) with n^μ and taking the spatial components of equation (3.47) respectively, gives the (3+1)-form of Ohm's law:

$$W\tilde{\rho}_{\text{el}} = \rho_{\text{el}} - \sigma u_\mu E^\mu, \tag{3.48}$$

$$J_i - \tilde{\rho}_{\text{el}} u_i = \sigma\left(W E_i + \epsilon_{ijk}\left(v^j + \beta^j\right) B^k u^t\right). \tag{3.49}$$

The approximation of ideal MHD is to assume that the **fluid is perfectly conducting**. Dividing (3.47) by σ and then taking the limit $\sigma \to \infty$ gives

$$F_{\mu\nu} u^\nu = 0, \tag{3.50}$$

or, in (3+1) form,

$$u_\mu E^\mu = 0 \tag{3.51}$$

and

$$\alpha E_i = -\epsilon_{ijk}\left(v^j + \beta^j\right) B^k. \tag{3.52}$$

Equation (3.51) means that the **electric field vanishes in the fluid's rest frame**. Using equation (3.52), equation (3.41) can be rewritten as

$$\mathcal{B}^i_{,t} = \left(v^i \mathcal{B}^j - v^j \mathcal{B}^i\right)_{,j}, \tag{3.53}$$

where $\mathcal{B}^i = \gamma^{1/2} B^i$ (cf. [3]).

3.3.4 Equations of Relativistic MHD

Even if electromagnetic fields are present, the continuity equation (3.24) or (3.33) holds unchanged. The only thing that changes in the hydrodynamic equations is the energy-momentum tensor $T^{\mu\nu}$ in (3.23), which now has to include both the fluid and the electromagnetic fields,

$$T^{\mu\nu} = T^{\mu\nu}_{\text{fluid}} + T^{\mu\nu}_{\text{em}}, \tag{3.54}$$

where

$$T^{\mu\nu}_{\text{em}} = \frac{1}{4\pi}\left(F^{\mu\rho}F^{\nu}_{\rho} - \frac{1}{4}g^{\mu\nu}F_{\rho\sigma}F^{\rho\sigma}\right) \tag{3.55}$$

(cf. e.g. [17]).

This gives rise to new terms in the energy equation (3.34) and the Euler equation (3.35), which become

$$\begin{aligned}\left(\gamma^{1/2}E\right)_{,t} + \left(\gamma^{1/2}Ev^j\right)_{,j} &= -P\left(\left(\gamma^{1/2}W\right)_{,t} + \left(\gamma^{1/2}Wv^j\right)_{,j}\right) \\ &\quad -\alpha\gamma^{1/2}u_\mu F^{\mu\nu}\mathcal{J}_\nu\end{aligned} \tag{3.56}$$

and

$$\begin{aligned}\left(\gamma^{1/2}S_i\right)_{,t} + \left(\gamma^{1/2}S_iv^j\right)_{,j} &= -\alpha\gamma^{1/2}\left(P_{,i} + \frac{S_\mu S_\nu}{2\alpha S^t}g^{\mu\nu}{}_{,i}\right) \\ &\quad +\alpha\gamma^{1/2}F_{i\mu}\mathcal{J}^\mu\end{aligned} \tag{3.57}$$

(cf. [3]).

Baumgarte and Shapiro [3] further show how to calculate the last term in equation (3.57), yielding as the final Euler equation

$$\begin{aligned}\left(\gamma^{1/2}S_i\right)_{,t} + \left(\gamma^{1/2}S_iv^j\right)_{,j} &= -\alpha\gamma^{1/2}\left(P_{,i} + \frac{S_\mu S_\nu}{2\alpha S^t}g^{\mu\nu}{}_{,i}\right) + \alpha\frac{\gamma^{1/2}}{4\pi}E_iE^j_{|j} \\ &\quad -\frac{\gamma^{1/2}}{4\pi}B^j\epsilon_{jik}\left(E^k_{,t} - \beta^lE^k_{,l} + E^l\beta^k_{,l} - \alpha KE^k\right) \\ &\quad -\frac{\gamma^{1/2}}{4\pi}B^j\left((\alpha B_j)_{,i} - (\alpha B_i)_{,j}\right).\end{aligned} \tag{3.58}$$

The new term in the energy equation (3.56) vanishes in the ideal MHD approximation according to equation (3.50), which will later be used in the simulation, thus leaving the energy equation of pure hydrodynamics (3.34) unchanged.

4 Hydrodynamic Collapse

In this section, the equations will be recast in terms of the specific coordinate system used in the numerical scheme and some results for the case of a collapsing star without any electromagnetic fields are shown.

4.1 Equations in Hernandez-Misner coordinates

In the absence of electromagnetic fields, the exterior of the star is pure vacuum and needs not to be evolved. In the interior it is most convenient to use a comoving radial coordinate A and two angular coordinates θ and φ which will be the usual spherical polar coordinates used due to the spherical symmetry of the problem. Defining in addition the circumferential radius $R(t, A)$, one can write the line element in the form, first introduced by Misner and Sharp [16],

$$ds^2 = -e^{2\phi(t,A)}dt^2 + e^{\lambda(t,A)}dA^2 + R^2(t,A)\left(d\theta^2 + \sin^2\theta d\varphi^2\right). \tag{4.1}$$

By comparing equation (4.1) with equation (3.1), the quantities used in the (3+1)-language for this particular coordinate system can be read off, i.e. the lapse function

$$\alpha_{\mathrm{MS}} = e^{\phi}, \tag{4.2}$$

the shift vector

$$\beta^i_{\mathrm{MS}} = 0, \tag{4.3}$$

and the metric on the spatial hypersurfaces defined by $t = \text{const.}$

$$\left[\gamma^{\mathrm{MS}}_{ij}\right] = \begin{pmatrix} e^{\lambda} & 0 & 0 \\ 0 & R^2 & 0 \\ 0 & 0 & R^2\sin^2\theta \end{pmatrix}, \tag{4.4}$$

which yields $\gamma_{\mathrm{MS}} = e^{\lambda}R^4\sin^2\theta$.

Since the spatial coordinates are comoving, only the t-component of the fluid's 4-velocity is nonzero and can be determined from the requirement $u_\mu u^\mu = -1$, yielding

$$\left[u^\mu_{\mathrm{MS}}\right] = \left(e^{-\phi}, 0, 0, 0\right). \tag{4.5}$$

The quantities used in the equations of relativistic hydrodynamics become

$$\begin{aligned} v^j_{\mathrm{MS}} &= 0, \\ W_{\mathrm{MS}} &= 1, \\ D_{\mathrm{MS}} &= \rho_0, \\ E_{\mathrm{MS}} &= \rho_0\epsilon, \\ S^{\mathrm{MS}}_i &= 0, \\ S^{\mathrm{MS}}_t &= e^{\phi}\rho_0 h. \end{aligned}$$

In addition, Misner and Sharp [16] define the total gravitational mass inside a radial coordinate A,

$$m = 4\pi \int_0^A \rho_0 \left(1+\epsilon\right) R^2 R_{,A} dA, \tag{4.6}$$

the comoving proper time derivative of the circumferential radius

$$U = u^\mu R_{,\mu} = e^{-\phi} R_{,t}, \tag{4.7}$$

hereafter simply called "velocity", and the quantity

$$\Gamma = e^{-\lambda/2} R_{,A}. \tag{4.8}$$

With the definitions of Γ and U, the Hamiltonian constraint (3.21) can be brought into the form

$$4\pi\rho_0 \left(1+\epsilon\right) R^2 R_{,A} = \frac{1}{2} e^{\lambda/2} \Gamma + \frac{1}{2} e^{\lambda/2} \Gamma U^2 + RUU_{,A} - \frac{1}{2} e^{\lambda/2} \Gamma^3 - R\Gamma\Gamma_{,A}, \tag{4.9}$$

which, with the definition of m, becomes

$$m_{,A} = \left(\frac{1}{2} R + \frac{1}{2} R U^2 - \frac{1}{2} R \Gamma^2 \right)_{,A}. \tag{4.10}$$

Integrating and solving for Γ yields

$$\Gamma = \left(1 + U^2 - \frac{2m}{R} \right)^{1/2}. \tag{4.11}$$

The momentum constraint (3.22) can be brought into the form

$$e^{-\phi} \lambda_{,t} = 2 \frac{U_{,A}}{R_{,A}}. \tag{4.12}$$

The equation of continuity (3.33) becomes

$$\left(\rho_0 e^{\lambda/2} R^2 \right)_{,t} = 0. \tag{4.13}$$

With the expression

$$\tilde{m}(A) = \int_0^A d\tilde{A} \int_0^\pi d\theta \int_0^{2\pi} d\varphi \rho_0 \gamma^{1/2} \tag{4.14}$$

for the rest mass $\tilde{m}$ enclosed within the coordinate A, one finds

$$\tilde{m}_{,A} = 4\pi \rho_0 e^{\lambda/2} R^2 \tag{4.15}$$

and therefore with equation (4.13)

$$\tilde{m}_{,At} = 0 \;\Leftrightarrow\; \tilde{m}_{,A} = \text{const.} \tag{4.16}$$

Choosing the coordinate A such that it denotes the rest mass,

$$A \equiv \tilde{m}, \tag{4.17}$$

the constant in equation (4.16) is one, and it can be solved for ρ_0, yielding

$$\rho_0 = \frac{\Gamma}{4\pi R^2 R_{,A}}. \tag{4.18}$$

Differentiating the definition of m, equation (4.6), with respect to A and using equation (4.18), one finds

$$m_{,A} = (1+\epsilon)\,\Gamma. \tag{4.19}$$

The energy equation (3.34) becomes in these coordinates

$$(\rho_0 \epsilon)_{,t} + \left(\frac{1}{2}\lambda_{,t} + \frac{2}{R}R_{,t}\right)(\rho_0 \epsilon + P) = 0. \tag{4.20}$$

Using the relation

$$\frac{1}{2}\lambda_{,t} + \frac{2}{R}R_{,t} = -\frac{1}{\rho_0}\rho_{0,t}, \tag{4.21}$$

which is obtained by carrying out the derivative in equation (4.13), this eventually becomes the first law of thermodynamics in the form

$$\epsilon_{,t} = -P\left(\frac{1}{\rho_0}\right)_{,t}. \tag{4.22}$$

Substituting the expressions for $\gamma_{\rm MS}$ and $S^{\mu}_{\rm MS}$, the A-component of the Euler equation (3.35) takes the form

$$\phi_{,A} = -\frac{1}{\rho_0 h}P_{,A}. \tag{4.23}$$

The $\theta\theta$-component of the evolution equation (3.20) becomes

$$\begin{aligned} 4\pi R^2\left(\rho_0\,(1+\epsilon) - P\right) \;=\; & e^{-\phi}\left(RR_{,t}e^{-\phi}\right)_{,t} + \frac{1}{2}e^{-2\phi}RR_{,t}\lambda_{,t} \\ & +1 - e^{-\lambda/2}\left(RR_{,A}e^{-\lambda/2}\right)_{,A} \\ & -e^{-\lambda}RR_{,A}\phi_{,A}. \end{aligned} \tag{4.24}$$

In this equation, $\lambda_{,t}$ can be replaced via equation (4.12) and $R_{,t}$ and $R_{,A}$ can be substituted by U and Γ. Then, after making use of equations (4.11) and (4.23), as well as the relation

$$e^{-\lambda/2} = 4\pi\rho_0 R^2, \tag{4.25}$$

which follows directly from equations (4.8) and (4.18), one can solve the resulting equation for $U_{,t}$. Thus, one finally obtains the evolution equation for the velocity

$$U_{,t} = -e^{\phi}\left(\frac{4\pi\Gamma R^2}{h}P_{,A} + \frac{m + 4\pi R^3 P}{R^2}\right). \tag{4.26}$$

Solving the definition of Γ, equation (4.8), for λ and substituting the result into equation (4.12), one obtains

$$e^{-\phi}\left(\ln\left(\frac{(R_{,A})^2}{\Gamma^2}\right)\right)_{,t} = 2\frac{U_{,A}}{R_{,A}}. \tag{4.27}$$

After substituting Γ with the expression (4.11) and carrying out the derivative with respect to t, one ends up with an equation containing $U_{,t}$. This can be replaced via equation (4.26). Furthermore, equation (4.23) can be used to replace $\phi_{,A}$ and equation (4.18) to replace ρ_0, leading to the final result

$$m_{,t} = -e^{\phi} 4\pi R^2 P U. \tag{4.28}$$

So finally, the ADM equations (3.19)-(3.22), as well as the continuity equation (3.33), the energy equation (3.34) and the Euler equation (3.35), have been transformed to the following set of seven partial differential equations, which needs to be supplemented by an equation of state $P = P(\epsilon, \rho_0)$:

$$U_{,t} = -e^{\phi}\left(\frac{4\pi\Gamma R^2}{h}P_{,A} + \frac{m + 4\pi R^3 P}{R^2}\right), \tag{4.29}$$

$$m_{,t} = -e^{\phi} 4\pi R^2 P U, \tag{4.30}$$

$$\phi_{,A} = -\frac{1}{\rho_0 h}P_{,A}, \tag{4.31}$$

$$\Gamma = \left(1 + U^2 - \frac{2m}{R}\right)^{1/2}, \tag{4.32}$$

$$\rho_0 = \frac{\Gamma}{4\pi R^2 R_{,A}}, \tag{4.33}$$

$$m_{,A} = (1 + \epsilon)\,\Gamma, \tag{4.34}$$

$$\epsilon_{,t} = -P\left(\frac{1}{\rho_0}\right)_{,t}. \tag{4.35}$$

Equations (4.29), (4.33), and (4.35) are also used by May and White [15], who use a slightly different form of equation (4.31) and instead of equation (4.30) use an equation similar to (4.27) and supplement these with the definitions of U and m.

Hernandez and Misner [11] replace the timelike coordinate t with a null coordinate u, which is constant along outgoing lightrays. This can be defined via

$$e^{\psi} du = e^{\phi} dt - e^{\lambda/2} dA, \tag{4.36}$$

yielding the new line element

$$ds^2 = -e^{2\psi}du^2 - 2e^{\psi}e^{\lambda/2}dudA + R^2\left(d\theta^2 + \sin^2\theta d\varphi^2\right). \tag{4.37}$$

The advantage of the null coordinate over the timelike coordinate is that the event horizon will correspond to $u = \infty$, so that the pathologies at the horizon will – in theory – not disturb the evolution of the equations outside of it. In practice however, as will be discussed in detail later, the numerical errors will make it impossible to conduct the hydrodynamic evolution arbitrarily close to the formation of the event horizon.

In the Hernandez-Misner coordinate system, the hypersurfaces defined by u = const. are not purely spatial. Therefore the terminology of the (3+1)-formulation cannot be directly used. Nevertheless it is possible to derive a set of equations in this coordinate system by transforming the equations as listed above in Misner-Sharp coordinates. Hernandez and Misner [11] (cf. also [4]) do this by transforming all derivatives according to the relations

$$e^{-\psi}\left.\frac{\partial}{\partial u}\right|_A = e^{-\phi}\left.\frac{\partial}{\partial t}\right|_A \tag{4.38}$$

and

$$\begin{aligned} e^{-\lambda/2}\left.\frac{\partial}{\partial A}\right|_u &= e^{-\lambda/2}\left(\left.\frac{\partial}{\partial A}\right|_t + \left.\frac{\partial t}{\partial A}\right|_u \left.\frac{\partial}{\partial t}\right|_A\right) \\ &= e^{-\lambda/2}\left.\frac{\partial}{\partial A}\right|_t + e^{-\phi}\left.\frac{\partial}{\partial t}\right|_A, \end{aligned} \tag{4.39}$$

which follow from equation (4.36).

Thus, the velocity becomes

$$U = e^{-\psi}R_{,u} \tag{4.40}$$

and the equations (4.30) and (4.33)-(4.35) can be transformed directly. Equation (4.29) contains the pressure gradient, which after the transformation becomes

$$\left.\frac{\partial P}{\partial A}\right|_t = \left.\frac{\partial P}{\partial A}\right|_u - e^{\lambda/2}e^{-\psi}\left.\frac{\partial P}{\partial u}\right|_A. \tag{4.41}$$

In order to have only the time derivative of U in the new evolution equation for U, the derivative of P with respect to u has to be replaced with an expressions that does not contain any u-derivatives. Writing the derivative as

$$P_{,u} = \left.\frac{\partial P}{\partial\left(\rho_0\left(1+\epsilon\right)\right)}\right|_s \left(\rho_0\left(1+\epsilon\right)\right)_{,u} + \left.\frac{\partial P}{\partial s}\right|_\epsilon s_{,u} \tag{4.42}$$

(cf. [11]), where s is the entropy, and assuming adiabatic changes, it becomes

$$P_{,u} = v_{\mathrm{s}}^2\left(\rho_0\epsilon_{,u} + \left(1+\epsilon\right)\rho_{0,u}\right), \tag{4.43}$$

where v_s is the sound speed. Replacing $\epsilon_{,u}$ via the new version of equation (4.35), one is left only with terms proportional to $\left(\rho_0^{-1}\right)_{,u}$ for which an expression is given in reference [11] which contains $U_{,u}$ as the only time derivative. So after inserting the final expression for $P_{,u}$ into the transformed version of equation (4.29), this can be solved for $U_{,u}$, making it the new evolution equation for U.

Equation (4.32) does not call for any transformation since it does not contain any derivatives and can therefore be used unchanged in the new coordinate system.

However, equation (4.31) needs to be replaced by an equation for $\psi_{,A}$. This can be found from the condition that du in equation (4.36) is a perfect differential, i.e.

$$\left(\frac{\partial}{\partial A}\left(\frac{\partial u}{\partial t}\right)\bigg|_A\right)\bigg|_t = \left(\frac{\partial}{\partial t}\left(\frac{\partial u}{\partial A}\right)\bigg|_t\right)\bigg|_A . \tag{4.44}$$

Taking the first derivatives

$$\left.\frac{\partial u}{\partial A}\right|_t = -e^{\lambda/2}e^{-\psi} \tag{4.45}$$

and

$$\left.\frac{\partial u}{\partial t}\right|_A = e^{\phi}e^{-\psi} \tag{4.46}$$

from equation (4.36) and carrying out the second derivatives, some terms can be replaced using equations (4.12) and (4.31). Then transforming the remaining derivatives and using equations (4.25) and (4.29), one arrives at an expression for $\psi_{,A}$.

Altogether, the new set of equations is

$$\begin{aligned} U_{,u} &= -\frac{e^{\psi}}{1-v_\mathrm{s}^2}\left(\frac{4\pi\Gamma R^2}{h}P_{,A} + \frac{m+4\pi R^3 P}{R^2}\right) \\ &\quad -\frac{e^{\psi}v_\mathrm{s}^2}{1-v_\mathrm{s}^2}\left(4\pi\rho_0 R^2 U_{,A} + \frac{2U\Gamma}{R}\right), \end{aligned} \tag{4.47}$$

$$m_{,u} = -e^{\psi}4\pi R^2 PU, \tag{4.48}$$

$$\psi_{,A} = \frac{1}{\Gamma}U_{,A} + \frac{m}{4\pi\rho_0 R^4\Gamma} + \frac{P}{\rho_0\Gamma R}, \tag{4.49}$$

$$\Gamma = \left(1 + U^2 - \frac{2m}{R}\right)^{1/2}, \tag{4.50}$$

$$\rho_0 = \frac{\Gamma + U}{4\pi R^2 R_{,A}}, \tag{4.51}$$

$$m_{,A} = (1+e)\,\Gamma - \frac{PU}{\rho_0}, \tag{4.52}$$

$$e_{,u} = -P\left(\frac{1}{\rho_0}\right)_{,u}, \tag{4.53}$$

where

$$v_{\mathrm{s}} = \left(\frac{1}{\rho_0^2 h}\left(P\left.\frac{\partial P}{\partial \epsilon}\right|_{\rho_0} + \rho_0^2\left.\frac{\partial P}{\partial \rho_0}\right|_{e}\right)\right)^{1/2} \tag{4.54}$$

is the speed of sound, which can be calculated via

$$v_s^2 = (\gamma - 1)\frac{h-1}{h} \tag{4.55}$$

for polytropic equations of state.

4.2 Numerical Implementation

The numerical implementation of the hydrodynamic evolution follows largely the scheme proposed by Baumgarte, Shapiro and Teukolsky [4]. The finite differencing of the equations (4.47) to (4.53) uses only central differences according to the scheme

$$y_{,x} = f(x, y, \dots) \longrightarrow \frac{y^{i+1} - y^i}{x^{i+1} - x^i} = f\left(x^{i+1/2}, y^{i+1/2}, \dots\right), \tag{4.56}$$

except for the spatial derivative of U appearing in equation (4.47), for which a van Leer scheme is used (cf. [10] and references therein). The van Leer scheme is derived from a general advection equation

$$d_{,t} + a d_{,x} = 0 \tag{4.57}$$

and gives

$$d^{n+1}_{i+1/2} = d^n_{i+1/2} - \sigma\left(d^{n+1/2}_{i+1/2} - d^{n+1/2}_{i-1/2} + \frac{1}{2}(1-\sigma)\left(\Delta^n_{i+1/2} - \Delta^n_{i-1/2}\right)\right) \tag{4.58}$$

as a finite difference representation of this equation, where

$$\sigma = a\frac{\Delta t}{\Delta x} \tag{4.59}$$

and

$$\Delta^n_{i-1/2} = \begin{cases} 2\frac{V^n_{i-1/2}}{d^n_{i+1/2} - d^n_{i-1/2}} & \text{if } V^n_{i-1/2} > 0 \\ 0 & \text{else} \end{cases}, \tag{4.60}$$

where

$$V^n_{i-1/2} = \left(d^n_{i-1/2} - d^n_{i-3/2}\right)\left(d^n_{i+1/2} - d^n_{i-1/2}\right) \tag{4.61}$$

(cf. [10]).

This reduces to a simple first order upwind scheme if the derivative of d changes sign, the benefit of which is that the second order terms are essentially

switched off when U is discontinuous and therefore better results are achieved in the presence of shocks.

In the case of equation (4.47), d corresponds to the velocity U and

$$\sigma = \frac{4\pi\rho_0 R^2 e^{\psi} v_s^2}{1 - v_s^2} \frac{\Delta u}{\Delta A}. \tag{4.62}$$

In addition, artificial viscosity is used (cf. e.g. [21]). This consists of a quantity Q, which is added to the pressure and is nonzero only if the fluid in the zone is compressed. In this case

$$Q = \kappa_1 \rho_0 \left(1 + \kappa_2 \epsilon\right) \left(\Delta U\right)^2, \tag{4.63}$$

where the coefficients $\kappa_1 = 1.5$ and $\kappa_2 = 0.3$ are used and ΔU is the difference of velocities at the inner and outer boundary of the zone. Artificial viscosity becomes important only if shocks are formed, in which case it is vital that the shockfront can still be resolved by the numerical grid. The additional pressure caused by the artificial viscosity ensures that the shock-front will always be smeared out over several gridzones in these cases. This is achieved here by defining the artificial viscosity as proportional to the square of the difference of velocities at the zone's boundaries.

The grid consists of 200 comoving radial gridpoints of which the inner two thirds are spaced equally with respect to the A-coordinate and the spacing decreases linearly over the outermost third of the gridpoints. Furthermore, all the geometric quantities $(R, U, m, A, e^{\psi}, \Gamma)$ are defined on gridpoints while all the thermodynamical quantities $(P, Q, \rho_0, \epsilon, h, v_{\mathrm{s}})$ are defined between gridpoints. Whenever the central differences call for a geometric quantity on half gridpoints or a thermodynamical quantity on gridpoints, they are linearly interpolated, with the exception of U and R for which a cubic interpolation is used because they are approximately proportional to the cubic root of the rest mass.

The only exception is the finite difference version of equation (4.49), which uses the smaller value R_i instead of the interpolated value $R_{i+1/2}$ in the denominator. This makes sure that the lapse function e^{ψ} calculated from equation (4.49) is never overestimated, thus eliminating the risk of a belated termination of the evolution scheme, which is taking place once the lapse function at the stellar surface falls below a certain value. The drawback is that the finite difference expression for the derivative $\left(e^{\psi}\right)_{,A}$ is then only first order accurate.

The timestep Δu used in the evolution scheme is not constant but is the same for all radial gridpoints. It is determined from four different conditions:

1. The Courant condition ensures that the local speed of sound is everywhere smaller than the grid velocity

$$v_{\mathrm{s}} < \frac{e^{\lambda/2}\Delta A}{e^{\phi}\Delta t} = \frac{e^{\lambda/2}\Delta A}{e^{\psi}\Delta u + e^{\lambda/2}\Delta A}, \tag{4.64}$$

where equation (4.36) has been used. This expression can be solved for Δu, yielding

$$\Delta u < \frac{1 - v_{\mathrm{s}}}{v_{\mathrm{s}}} \frac{\Delta R}{e^{\psi}\,(\Gamma + U)}. \tag{4.65}$$

2. The rest-mass density ρ_0 is required to change by less than 2% within one timestep.

3. The circumferential radius R is required to change by less than 0.5% within one timestep.

4. The quantity $(1 - 2m/R)$ is required to change by less than 10% within one timestep.

The full set of finite difference equations can be found in the appendix and is very similar to the one presented in reference [4].

The boundary conditions used at the center of the star are

$$U(A = 0) = 0, \tag{4.66}$$

$$m(A = 0) = 0 \tag{4.67}$$

and

$$\Gamma(A = 0) = 1. \tag{4.68}$$

At the stellar surface the pressure is vanishing by definition

$$P(A = A_{\max}) = 0 \tag{4.69}$$

and the lapse function e^{ψ} on the surface is chosen as

$$e^{\psi}(A = A_{\max}) = \Gamma + U, \tag{4.70}$$

such that the null coordinate u in the interior of the star is matched to the Schwarzschild coordinate t in the exterior, thus giving the interpretation that the u-coordinate of an event is the proper time of an observer at spatial infinity when he/she is observing the event.

In every scenario of interest the star can be assumed to be at rest initially, making it easy to find appropriate initial data on a spatial surface defined by $t = \text{const}$. However, the numerical evolution scheme works with the non-spatial hypersurfaces defined by $u = \text{const}$. This is taken into account only in the easiest case of the Oppenheimer-Snyder collapse. Otherwise, the star is taken to be at rest on the initial hypersurface $u = 0$ as an approximation. Since the fluid velocity in the shaded region of Figure 1 will be almost zero, the actual profile of the star on the $(u = 0)$-hypersurface will be very similar to the one on the $(t = 0)$-hypersurface. Therefore the error introduced by this approximation should be very small. Actually, as will be discussed later, the numerical results using this assumption are in good agreement with the analytic ones in the case of dust collapse and the comparison with an alternative numerical scheme shows a good agreement in the case of polytropic stars (cf. section 4.5.1).

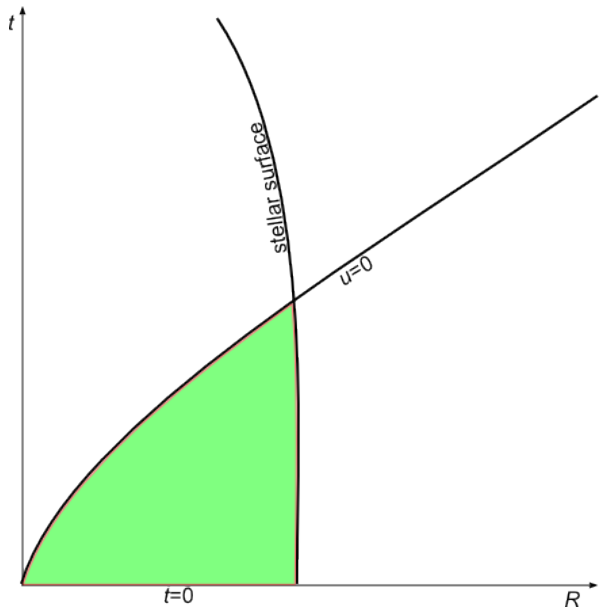

Figure 1: Schematic space-time diagram showing the initial spacelike hypersurface defined by $t = 0$ and the initial null hypersurface defined by $u = 0$, as well as the stellar surface. The effects of the shaded region are ignored in the numerical simulations due to the choice of initial data (see text for details).

4.3 Testbed Calculations

In order to check whether the numerical scheme produces reasonable results it was applied to two pressureless scenarios for which the analytic solution is known. The first scenario is the Oppenheimer-Snyder collapse which consists of a homogeneous collapsing ball of dust. The second one is the Tolman-Bondi collapse, in which the density-profile of the sphere of dust is chosen in a non-trivial way.

4.3.1 Oppenheimer-Snyder collapse

The **analytic solution** of the collapsing homogeneous dustball is given by the Friedmann metric

$$ds^2 = -d\tau^2 + a^2(\tau)\left(d\chi^2 + \sin^2\chi\left(d\theta^2 + \sin^2\theta d\varphi^2\right)\right), \tag{4.71}$$

where χ is a comoving radial coordinate, together with the equations describing the worldlines of the dust particles as a function of the conformal time η

$$a = a_0\left(1 + \cos\eta\right), \tag{4.72}$$

$$\tau = a_0\left(\eta + \sin\eta\right) \tag{4.73}$$

(cf. e.g. [17]). Here, the surface of the star corresponds to some finite value $0 \leq \chi_0 \leq \pi$ and the conformal time ranges from $\eta = 0$ to $\eta = \pi$. The

circumferential radius is given by

$$R = a \sin \chi. \tag{4.74}$$

The Friedmann coordinates can be transformed to a system containing an outgoing null coordinate similar to Hernandez-Misner coordinates using the relation

$$e^{\psi} du = d\tau - a d\chi, \tag{4.75}$$

which leads to the line element

$$ds^2 = -e^{2\psi} du^2 - 2e^{\psi} a du d\chi + a^2 \sin^2 \chi \left(d\theta^2 + \sin^2 \theta d\varphi^2 \right). \tag{4.76}$$

Using this transformation and matching the interior to the exterior at the stellar surface, where the exterior is described by the Schwarzschild metric

$$ds^2 = -\left(1 - \frac{2M}{R}\right) dt^2 + \left(1 - \frac{2M}{R}\right)^{-1} dR^2 + R^2 \left(d\theta^2 + \sin^2 \theta d\varphi^2 \right) \tag{4.77}$$

and the stellar surface follows a geodesic according to

$$R_{\text{surf}} = \frac{R_{\text{surf},0}}{2} \left(1 + \cos \eta\right) \tag{4.78}$$

and

$$\tau = \left(\frac{R_{\text{surf},0}^3}{8M} \right)^{1/2} \left(\eta + \sin \eta \right), \tag{4.79}$$

it is shown in reference [4] that the relation between the conformal time η and the outgoing null coordinate u is given, at $\chi = 0$, by the differential equation

$$\frac{\partial u \left(\chi = 0, \eta \right)}{\partial \eta} = a_0 \frac{\cos \chi_0 \left(1 + \cos \left(\eta + \chi_0 \right)\right) + \sin \chi_0 \sin \left(\eta + \chi_0 \right)}{1 - \frac{2 \sin^2 \chi_0}{1 + \cos(\eta + \chi_0)}}. \tag{4.80}$$

Integrating gives the function $u(\chi = 0, \eta)$. This can be inverted, giving a function

$$\eta_0(u) := \eta(\chi = 0, u). \tag{4.81}$$

From equation (4.75) it can be seen that $d\chi = d\eta$ on surfaces of constant u, which yields the general dependence of η on u and χ

$$\eta(u, \chi) = \eta_0(u) + \chi. \tag{4.82}$$

With this relation, all quantities of interest can be expressed as functions of u and χ, namely

$$R(u, \chi) = a_0 \left(1 + \cos \left(\eta_0(u) + \chi \right)\right) \sin \chi, \tag{4.83}$$

$$e^{\psi(u,\chi)} = \frac{\left(1 + \cos \left(\eta_0(u) + \chi \right)\right) \left(1 - \frac{2 \sin^2 \chi_0}{1 + \cos(\eta_0(u) + \chi_0)} \right)}{\cos \chi_0 \left(1 + \cos \left(\eta_0(u) + \chi_0 \right)\right) + \sin \chi_0 \sin \left(\eta_0(u) + \chi_0 \right)}, \tag{4.84}$$

$$\tau(u, \chi) = a_0 \left(\eta_0(u) + \chi + \sin \left(\eta_0(u) + \chi \right) \right), \tag{4.85}$$

$$U(u,\chi) = -\sin\chi \frac{\sin\left(\eta_0(u)+\chi\right)}{1+\cos\left(\eta_0(u)+\chi\right)}, \tag{4.86}$$

$$\rho_0(u,\chi) = \frac{3}{4\pi a_0^2}\left(\frac{1}{1+\cos\left(\eta_0(u)+\chi\right)}\right)^3. \tag{4.87}$$

In order to be able to compare these analytic results to the numerical ones, one needs to find a relation between the Friedmann coordinate χ and the Hernandez-Misner coordinate A. This can be derived by equating (4.37) and (4.76), which leads to

$$e^{\lambda/2}dA = a d\chi. \tag{4.88}$$

Using equation (4.25), as well as (4.72), (4.74), and (4.87), one finds

$$dA = 3a_0 \sin^2\chi d\chi. \tag{4.89}$$

This can be integrated, yielding the required relation

$$A = \frac{3}{2}a_0\left(\chi - \sin\chi\cos\chi\right), \tag{4.90}$$

which, after inverting, makes it possible to express the quantities of equations (4.83)-(4.87) as functions of u and A.

In the case of the Oppenheimer-Snyder collapse, where the analytic solution is known, it is easily possible to use the exact **initial data** on the hypersurface defined by $u = 0$. Since the star collapses from rest at $\eta = 0$, it is reasonable to use

$$\eta_0(u=0) = 0 \tag{4.91}$$

for the initial data. This means that the null-points of the conformal time η and the Hernandez-Misner coordinate u coincide in the center of the star.

Inserting (4.91) into equations (4.83)-(4.87), the appropriate initial data

$$U_{\text{init}} = -\frac{\sin^2\chi}{1+\cos\chi}, \tag{4.92}$$

$$\rho_{0,\text{init}} = \frac{3}{4\pi a_0^2}\left(\frac{1}{1+\cos\chi}\right)^3, \tag{4.93}$$

$$e^{\psi_{\text{init}}} = \frac{(1+\cos\chi)\left(1-\frac{2\sin^2\chi_0}{1+\cos\chi_0}\right)}{\cos\chi_0\left(1+\cos\chi_0\right)+\sin^2\chi_0}, \tag{4.94}$$

$$R_{\text{init}} = a_0\left(1+\cos\chi\right)\sin\chi, \tag{4.95}$$

$$\tau_{\text{init}} = a_0\left(\chi+\sin\chi\right) \tag{4.96}$$

are obtained as functions of χ. These are then calculated in dependence on the A-coordinate by inverting equation (4.90) numerically.

From these quantities the initial distribution of gravitational mass can be calculated by integrating equation (4.52) with $e = P = 0$, according to

$$m(A=0) = 0 \tag{4.97}$$

and

$$\begin{aligned} m(A) &= \int_0^A \Gamma d\tilde{A} \\ &= \int_0^A \left(\rho_0 4\pi R^2 R_{,\tilde{A}} - U\right) d\tilde{A} \\ &= \frac{4\pi}{3}\int_0^{R^3(A)} \rho_0 d\left(\tilde{R}^3\right) - \int_0^A U d\tilde{A}, \end{aligned} \tag{4.98}$$

where equation (4.25) has been used.

With the above system of equations and initial data, we conducted several **numerical simulations** using different sets of total mass M and initial circumferential radius $R_{\mathrm{surf},0}$ of the stellar surface. From these given values, a_0 and χ_0 can be calculated analytically according to

$$a_0 = \left(\frac{R_{\mathrm{surf},0}^3}{8M}\right)^{1/2} \tag{4.99}$$

and

$$\sin\chi_0 = \left(\frac{2M}{R_{\mathrm{surf},0}}\right)^{1/2}. \tag{4.100}$$

These relations arise from equating the expressions for the motion of the stellar surface parameterized by η in Friedmann and Schwarzschild coordinates.

For all sets of parameters, the results obtained with our numerical code match the analytic ones excellently. In Figure 2, both the numerical result and the analytic solution for the proper time of the mass-shells in dependence of the circumferential radius are shown for different values of the Hernandez-Misner coordinate u, where the analytic and numerical results are represented by solid lines and crosses, respectively. The parameters used are the same values used in reference [4], namely $R_{\mathrm{surf},0} = \sqrt{1.6}$ and $M = R_{\mathrm{surf},0}/5$.

In a similar way, Figures 3 to 5, show the velocity U, the rest-mass density ρ_0, and the lapse function e^{ψ}, respectively. It is evident that the numerical and analytic solutions are in agreement for all variables. Furthermore, it can be seen that the stellar surface will approach the event horizon at $R = 2M$ for $u \to \infty$.

4.3.2 Tolman-Bondi Collapse

The Tolman-Bondi scenario is the collapse of a dust sphere ($P = 0$) with a non-trivial radial density profile. The density profile is chosen here to be the same as in reference [4], i.e.

$$\rho_0 = \frac{1}{8\pi} e^{-4R^2}. \tag{4.101}$$

In this case the aforementioned approximation is made that the data for the star at rest are taken as **initial data** on the $(u = 0)$-surface, so

$$U = 0 \tag{4.102}$$

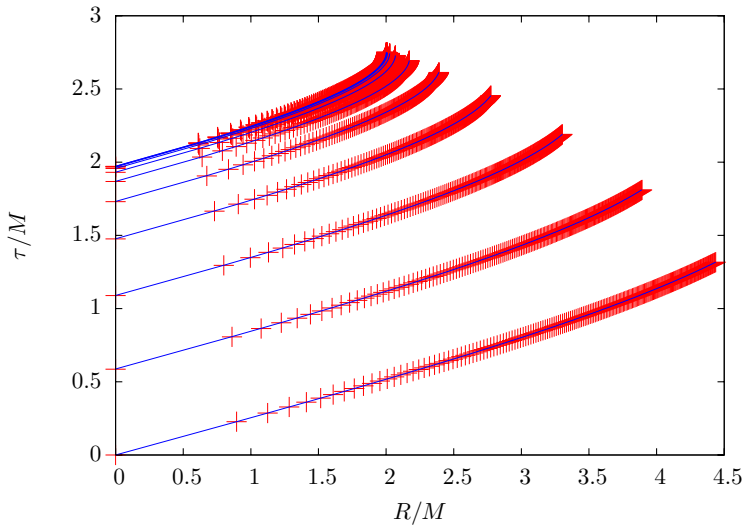

Figure 2: Proper time τ vs. circumferential radius R for the Oppenheimer-Snyder collapse with $R_{\mathrm{surf},0} = \sqrt{1.6}$ and $M = R_{\mathrm{surf},0}/5$. The numerical results are represented by crosses, the analytic solution by solid lines. The lines correspond (from bottom to top) to $u = 0, 1, 2, 3, 4, 5, 6, 7, 8, 9, 10$.

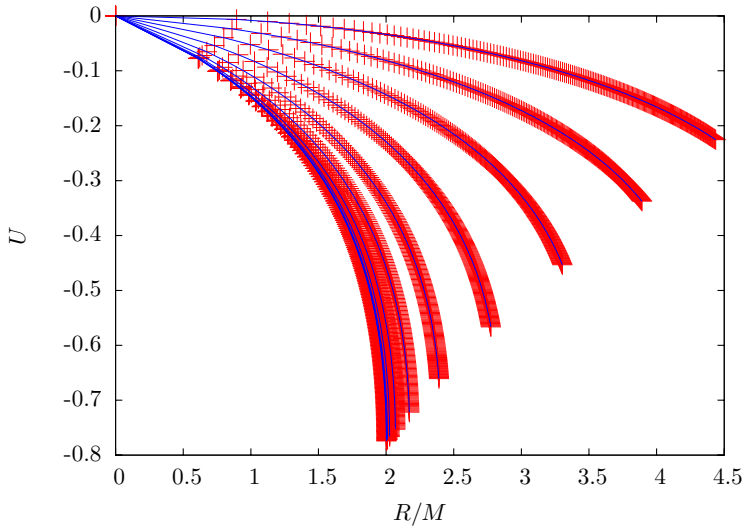

Figure 3: Velocity U vs. circumferential radius R for the Oppenheimer-Snyder collapse with $R_{\mathrm{surf},0} = \sqrt{1.6}$ and $M = R_{\mathrm{surf},0}/5$. The numerical results are represented by crosses, the analytic solution by solid lines. The lines correspond (from top to bottom) to $u = 0, 1, 2, 3, 4, 5, 6, 7, 8, 9, 10$.

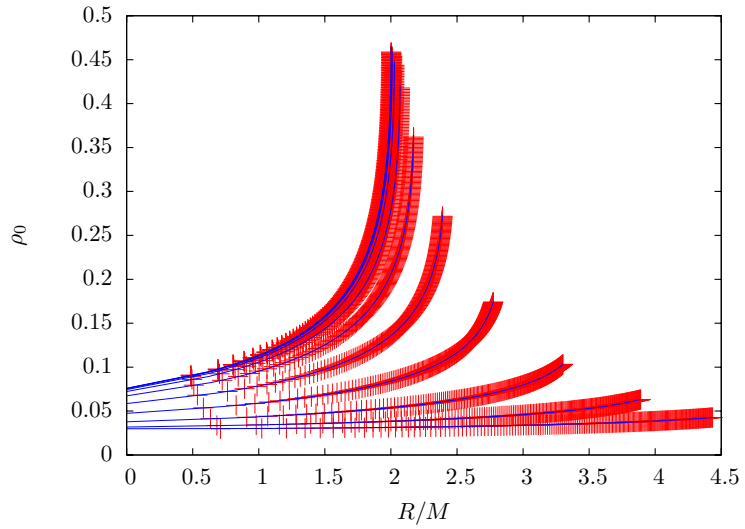

Figure 4: Rest-mass density ρ_0 vs. circumferential radius R for the Oppenheimer-Snyder collapse with $R_{\mathrm{surf},0} = \sqrt{1.6}$ and $M = R_{\mathrm{surf},0}/5$. The numerical results are represented by crosses, the analytic solution by solid lines. The lines correspond (from bottom to top) to $u = 0, 1, 2, 3, 4, 5, 6, 7, 8, 9, 10$.

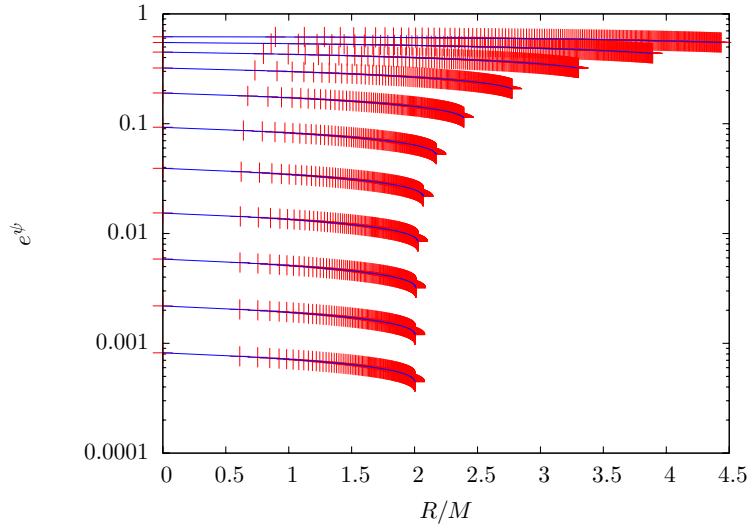

Figure 5: Lapse function e^{ψ} vs. circumferential radius R for the Oppenheimer-Snyder collapse with $R_{\mathrm{surf},0} = \sqrt{1.6}$ and $M = R_{\mathrm{surf},0}/5$. The numerical results are represented by crosses, the analytic solution by solid lines. The lines correspond (from top to bottom) to $u = 0, 1, 2, 3, 4, 5, 6, 7, 8, 9, 10$.

and

$$\tau = 0 \tag{4.103}$$

throughout the star.

Using $U = 0$ and equation (4.101) in equation (4.51), one finds

$$R_{,A} = \frac{2\Gamma}{R^2} e^{4R^2}. \tag{4.104}$$

Equation (4.50) with $U = 0$ becomes

$$\Gamma = \left(1 - \frac{2m}{R}\right)^{1/2}. \tag{4.105}$$

Using $\epsilon = 0$ and equation (4.101) in equation (4.6), the expression for the total gravitational mass becomes

$$m = -\frac{R}{16} e^{-4R^2} + \frac{\sqrt{\pi}}{64} \mathrm{erf}\,(2R)\,. \tag{4.106}$$

Substituting the expressions (4.105) and (4.106) into equation (4.104),

$$R_{,A} = \frac{2e^{4R^2}}{R^2} \left(1 + \frac{1}{R}\left(\frac{R}{8} e^{-4R^2} - \frac{\sqrt{\pi}}{32} \mathrm{erf}\,(2R)\right)\right)^{1/2} \tag{4.107}$$

is obtained. Given the initial circumferential radius of the stellar surface $R_{\mathrm{surf},0}$, the inverse of the last expression can be integrated to yield the A-coordinate of the stellar surface according to

$$A_{\max} = \int_0^{A_{\max}} dA = \int_0^{R_{\mathrm{surf},0}} \left(R_{,A}\right)^{-1} dR. \tag{4.108}$$

Once $A_{\max}$ has been found, the intermediate A-coordinates are assigned to the gridpoints such that the inner two thirds are spaced equally with respect to the A-coordinate and the spacing decreases linearly over the outermost third of the gridpoints. After that, the initial circumferential radii of the gridpoints can be integrated according to

$$R(A) = \int_0^A R_{,\tilde{A}} d\tilde{A}, \tag{4.109}$$

using the above expression for $R_{,A}$. The initial distribution of the gravitational mass is then calculated using equation (4.106) and the density profile using equation (4.101).

Finally, the initial lapse function can be calculated from the boundary condition

$$e^{\psi}\left(A_{\max}\right) = \Gamma\left(A_{\max}\right) = \left(1 - \frac{2M}{R_{\mathrm{surf},0}}\right)^{1/2} \tag{4.110}$$

and by integrating equation (4.49) from the surface inward.

The **analytic solution** for the worldlines of the mass-shells is given in parameterized form by

$$R(\eta, A) = -\frac{F(A)}{2f(A)}\left(1 - \cos\eta\right) \tag{4.111}$$

and

$$\tau_0(A) - \tau(A, \eta) = \frac{F(A)}{2\left(-f(A)\right)^{3/2}}\left(\eta - \sin\eta\right) \tag{4.112}$$

(cf. [13]), where η runs from π to 0 as the star collapses from rest to the singularity. The three functions F, f, and τ_0 are determined by the initial configuration according to

$$8\pi\rho_0 = \frac{F_{,A}}{R_{,A}R^2}, \tag{4.113}$$

$$\left(R_{,\tau}\right)^2 = f + \frac{F}{R} \tag{4.114}$$

(cf. [13]) and by

$$\tau(\eta = \pi) = 0. \tag{4.115}$$

Using the initial density profile (4.101), equation (4.113) becomes

$$F_{,R} = R^2 e^{-4R^2}, \tag{4.116}$$

which in integrated form reads

$$F = -\frac{R}{8}e^{-4R^2} + \frac{\sqrt{\pi}}{32}\mathrm{erf}\left(2R\right). \tag{4.117}$$

Using $\frac{\partial R}{\partial \tau}\big|_{\tau=0} = 0$, equation (4.114) yields the expression for f as

$$f = -\frac{F}{R}. \tag{4.118}$$

Finally, substituting equation (4.115) into equation (4.112) gives

$$\tau_0 = \frac{\pi F}{2\left(-f\right)^{3/2}}. \tag{4.119}$$

Then, together with the relationship between the circumferential radius R and the A-coordinate given in equation (4.107), the worldline of each mass-shell, i.e. its τ- and R-coordinates, are known as functions of the parameter η.

The parameter used in the **numerical simulation** of the Tolman-Bondi collapse is again $R_{\mathrm{surf},0} = \sqrt{1.6}$. The numerical evolution was terminated once the lapse function at the surface became very small, $e^{\psi_{\mathrm{surf}}} < 10^{-3}$, i.e. when the stellar surface came close to the event horizon at $R = 2M$.

Figure 6 shows both the numerical result and the analytic result for the worldlines of several mass shells. Once again, both solutions agree very well. This shows not only that the numerical evolution scheme is accurate but also that the error introduced by taking the static configuration as initial data on a surface of constant u is small.

Note that while the numerical evolution terminates before the stellar surface passes the event horizon, the analytic solution continues until $R_{\mathrm{surf}} = 0$.

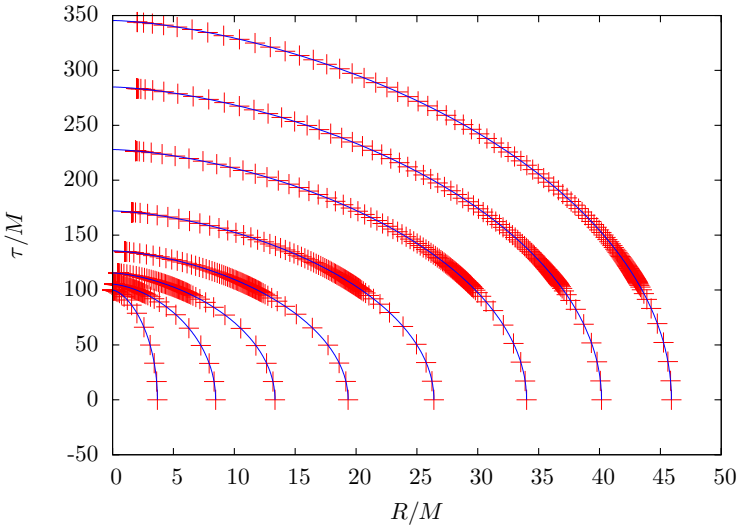

Figure 6: Worldlines of several mass-shells in the proper time vs. circumferential radius plane for the Tolman-Bondi collapse. The initial density profile is given by $\rho_0 = \frac{1}{8\pi} e^{-4R^2}$ and the initial circumferential radius of the stellar surface is $R_{\mathrm{surf},0} = \sqrt{1.6}$. The numerical results are represented by crosses, the analytic solution by solid lines. The outermost mass-shell that is shown corresponds to the stellar surface.

4.4 Collapse of a Polytropic Star

To model a more realistic star, a polytropic equation of state

$$P = K\rho_0^\gamma \tag{4.120}$$

is assumed, where the adiabatic index γ is given by

$$\gamma = 1 + \frac{1}{n} \tag{4.121}$$

and n is called the polytropic index. In this case the approximation is made again that the configuration at rest is taken as **initial data** on the $(u = 0)$-surface.

The equilibrium configurations, which are the initial stellar models, are governed by the Oppenheimer-Volkoff equation (cf. e.g. [17])

$$P_{,R} = -\frac{(\rho_0 (1+\epsilon) + P)\left(4\pi R^3 P + m\right)}{R\,(R-2m)}. \tag{4.122}$$

In this equation, the pressure P can be expressed through the rest-mass density ρ_0 via the equation of state (4.120). So it is useful to express the internal energy ϵ also as a function of ρ_0.

The first law of thermodynamics (4.35) can be rewritten using equation (4.120) to become

$$\epsilon_{,t} = K\rho_0^{\gamma-2}\rho_{0,t}, \tag{4.123}$$

which, under the assumption that ϵ is a function of ρ_0 only, becomes

$$\epsilon_{,\rho_0} = K\rho_0^{\gamma-2}. \tag{4.124}$$

This can be integrated to yield

$$\epsilon = \frac{K}{\gamma-1}\rho_0^{\gamma-1}. \tag{4.125}$$

Substituting (4.120) and (4.125) into equation (4.122) and adding the equation obtained by differentiating the definition of m, equation (4.6), with respect to R, one obtains a system of two ordinary differential equations:

$$\frac{\partial\rho_0}{\partial R} = -\frac{\left(\rho_0\left(1+\frac{K}{\gamma-1}\rho_0^{\gamma-1}\right) + K\rho_0^\gamma\right)\left(4\pi R^3 K\rho_0^\gamma + m\right)}{K\gamma\rho_0^{\gamma-1}R\,(R-2m)}, \tag{4.126}$$

$$\frac{\partial m}{\partial R} = 4\pi\rho_0\left(1+\frac{K}{\gamma-1}\rho_0^{\gamma-1}\right)R^2. \tag{4.127}$$

To obtain an equilibrium configuration, first a polytropic index n and a proportionality constant K, as well as a central density $\rho_{0,\mathrm{centr}} = \rho_0(R=0)$ are chosen. Then the equations (4.126) and (4.127) are integrated using a 4^{th} order Runge-Kutta scheme, which gives the functions $\rho_0(R)$ and $m(R)$. The

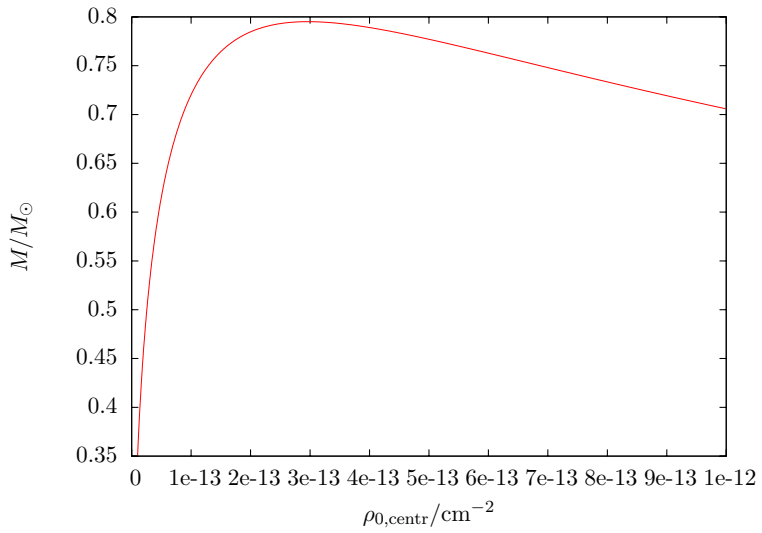

Figure 7: Total gravitational mass vs. central density for equilibrium models with $n = 1.5$ and $K = 5.38 \times 10^9$ cm^4 g$^{-2/3}$ s^{-2}.

functions $P(R)$ and $\epsilon(R)$ can then be calculated directly from equation (4.120) and (4.125) respectively.

Figure 7 shows the results for the total gravitational mass M in dependence of the central density $\rho_{0,\mathrm{centr}}$ for equilibrium models with $n = 1.5$ and $K = 5.38 \times 10^9$ cm^{4}g$^{-2/3}$s^{-2}. The maximum mass is obtained at a central density of about $\rho_{0,\mathrm{centr}} \approx 2.95 \times 10^{-13}$ cm^{-2}. For configurations with a lower central density, stability is to be expected and configurations with a higher central density are expected to collapse (cf. [22]).

Once the four quantities ρ_0, m, P and ϵ are known as functions of the circumferential radius, the relation between the radial comoving coordinate A and the circumferential radius R is needed to adjust the initial data with the coordinates of our code for stellar collapse. This is obtained by integrating

$$A_{,R} = (R_{,A})^{-1} = \frac{4\pi\rho_0 R^2}{\left(1 - \frac{2m}{R}\right)^{1/2}} \tag{4.128}$$

with the boundary condition $A(R = 0) = 0$. The last equality follows directly from equations (4.32) and (4.33) with $U = 0$. The resulting function $A(R)$ can then be inverted, leading to the dependence of ρ_0, m, P and ϵ on A.

The initial sound speed $v_\mathrm{s}(A)$ and enthalpy $h(A)$ can then be calculated directly from their definitions. Finally, the initial lapse function is calculated by integrating equation (4.49) with the appropriate boundary condition at the stellar surface and the quantities U, τ and Q are set to zero throughout the star.

Figure 8 shows the worldlines of several mass-shells for the collapse of a fluid with a polytropic equation of state obtained from the **numerical sim-**

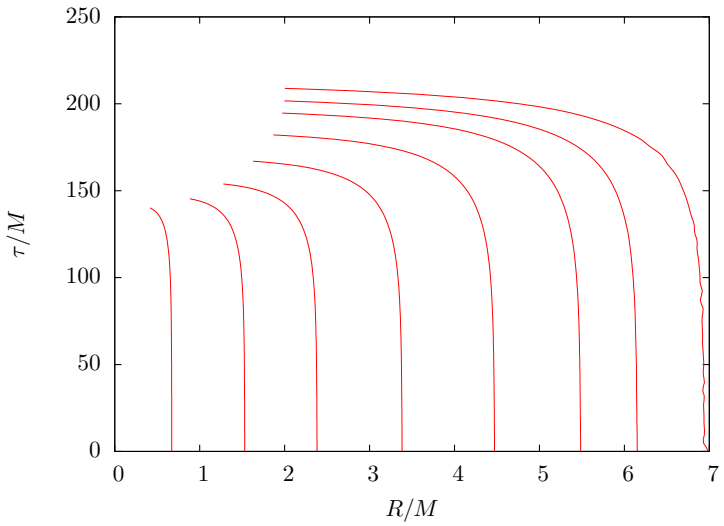

Figure 8: Worldlines of several mass-shells for the collapse of a polytrope with $n = 1.5$, $K = 5.38 \times 10^9$ cm^{4}g$^{-2/3}$s^{-2} and a central density of $\rho_{0,\mathrm{centr}} = 5.0 \times 10^{15}$ g cm^{-3}. The outermost mass-shell that is shown corresponds to the stellar surface.

ulation. The parameters used are $n = 1.5$ and $K = 5.38 \times 10^9$ cm^{4}g$^{-2/3}$s^{-2}, which are the parameters for a completely degenerate nonrelativistic neutron gas. The central density was chosen to be $\rho_{0,\mathrm{centr}} = 5.0 \times 10^{15}$ g cm^{-3} which corresponds to about 3.85×10^{-13} cm^{-2}. Thus it is clearly above the critical central density, with which the stellar mass is maximized, and the collapse is expected to happen. Again, the numerical evolution was stopped once $e^{\psi_{\mathrm{surf}}} < 10^{-3}$ was satisfied. It can be seen in the picture that this corresponds to the time when the stellar surface comes close to the event horizon at $R = 2M$.

4.5 Further Numerical Tests

4.5.1 Influence of Initial Hypersurface

As mentioned earlier, the approximation is made that the configuration at rest is taken as initial data on the $(u = 0)$-surface instead of the $(t = 0)$-surface. In order to test the quality of this approximation, the same initial configuration was evolved on the one hand using the numerical scheme described before and using a scheme based on the equations in Misner-Sharp coordinates on the other hand. The latter scheme uses hypersurfaces of constant timelike coordinate t as timesteps and therefore the aforementioned approximation for the initial data is not needed. Figure 9 shows the results for both numerical schemes. The initial model used is the same as in Figure 8. It is clear that the difference in the worldlines between the two schemes is only marginal. Further-

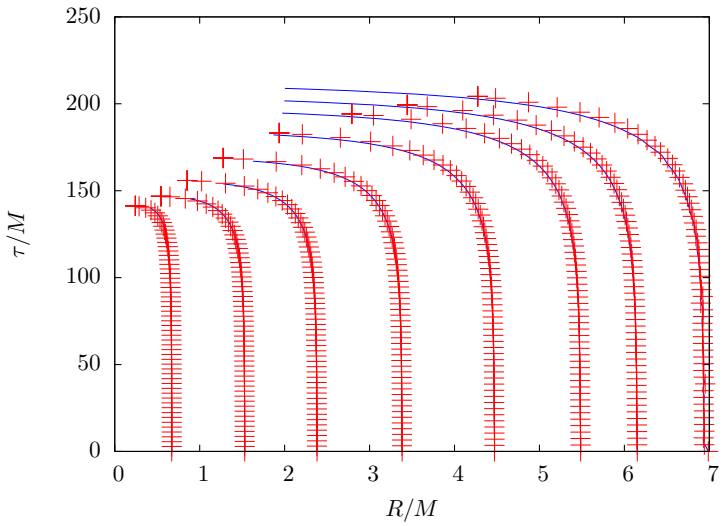

Figure 9: Worldlines of several mass-shells for a collapsing polytropic star. The model used is the same shown in Figure 8. The solid lines depict the worldlines as calculated with the Hernandez-Misner scheme, the crosses depict the worldlines as calculated with a Misner-Sharp scheme.

more, the advantage of using the null coordinate u becomes obvious. While the Misner-Sharp scheme (crosses) penetrates the event horizon in the interior of the star and then breaks down quickly, the Hernandez-Misner scheme (lines) stays clear of it and can therefore be continued until all mass-shells have come close to the newly formed horizon.

4.5.2 Finding the Onset of Instability

To see whether the cirtical central density, which is determined from Figure 7 as $\rho_{0,\mathrm{centr}} \approx 2.95 \times 10^{-13}$ cm^{-2}, does indeed seperate the collapsing models from the stable ones when evolved numerically, the numerical evolution was carried out for various equilibrium models with different central densities.

The results confirm the value for the critical central density. Figure 10 shows the worldlines of two models, one having a central density a little below the critical one (solid lines) and the other having a central density slightly above the critical one (dashed lines). It can be seen that the latter model collapses while the former roughly keeps its initial circumferential radius, i.e. the star is oscillating around the initial equilibrium model.

4.5.3 Oscillation Frequencies

In a stable configuration, numerical inaccuracies excite radial oscillations. This can be seen in the results represented by solid lines in Figure 10. To determine the frequencies of these oscillations, the evolution of the rest-mass density

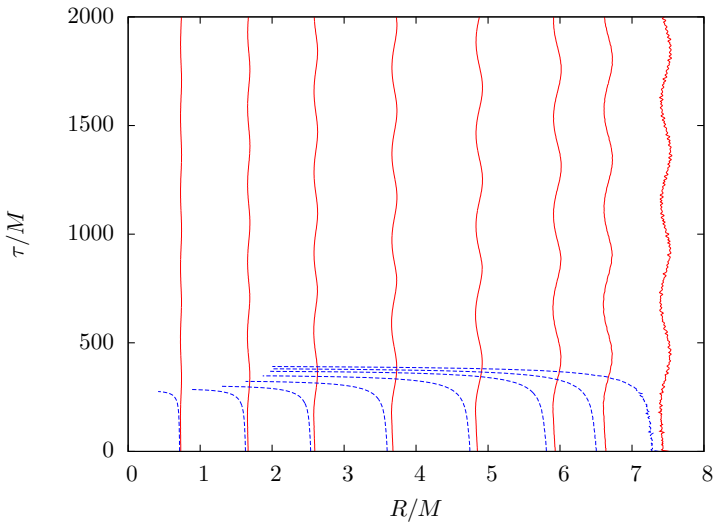

Figure 10: Worldlines of several mass-shells for two polytropic models with $n = 1.5$ and $K = 5.38 \times 10^9$ cm^{4}g$^{-2/3}$s^{-2}. The solid lines correspond to a model with a central density of $\rho_{0,\mathrm{centr}} = 2.85 \times 10^{-13}$ cm^{-2}, the dashed lines to a model with a central density of $\rho_{0,\mathrm{centr}} = 3.05 \times 10^{-13}$ cm^{-2}. The outermost mass-shells that are shown correspond to the stellar surfaces.

at some point in the interior of the star was monitored and then Fourier transformed. This treatment was applied to some models with polytropic equations of state that were also used in reference [12]. However, the polytropic equations of state used in reference [12] are of the form

$$P = K\rho^\gamma, \tag{4.129}$$

where

$$\rho = \rho_0 \left(1 + \epsilon\right), \tag{4.130}$$

so the code had to be changed a little in order to make the comparison possible. At last, we find that the obtained frequencies for $K = 2 \times 10^5$ km^2 and $\gamma = 3.0$ with central densities of $\rho_{\mathrm{centr}} = 0.8,\ 1.0,\ 1.2,\ 1.4 \times 10^{15}$ g cm^{-3} are the same as the ones provided in the appendix of reference [12]. Thus we can say that the oscillation seen in Figure 10 is indeed just a radial oscillation.

4.5.4 Long-term Stability

To test the long-term stability of the code, a stable configuration was evolved for a long time. The evolution could be continued until $\tau_{centr} \gtrsim 2 \times 10^4 M$ without any detectable change in the configuration – apart from the aforementioned oscillations. We believe that this evolution time is enough to see the stability of our code and coclude that our code is stable for long-term evolutions.

4.5.5 Determining the Order of Accuracy

The local truncation error of the central difference method employed is of second order in the stepwidth. This can be seen from Taylor's theorem as follows. Assume a function $y(x)$, which is three times differentiable on an interval containing two points x_i and $x_{i+1} = x_i + h$. Then the central difference formula for the drivative $y_{,x}$ in the point $x_{i+1/2} = (x_i + x_{i+1})/2$ is expressed as

$$(y_{,x})^{(\mathrm{c.d.})}_{i+1/2} = \frac{y_{i+1} - y_i}{h}. \tag{4.131}$$

According to Taylor's theorem, there exist numbers χ_1 and χ_2 with $x_i < \chi_1 < x_{i+1/2} < \chi_2 < x_{i+1}$ such that

$$\begin{aligned} y_i &= y_{i+1/2} - (y_{,x})_{i+1/2} \frac{h}{2} + \frac{1}{2} (y_{,xx})_{i+1/2} \left(\frac{h}{2}\right)^2 \\ &\quad -\frac{1}{6} y_{,xxx}(x = \chi_1) \left(\frac{h}{2}\right)^3 \end{aligned} \tag{4.132}$$

and

$$\begin{aligned} y_{i+1} &= y_{i+1/2} + (y_{,x})_{i+1/2} \frac{h}{2} + \frac{1}{2} (y_{,xx})_{i+1/2} \left(\frac{h}{2}\right)^2 \\ &\quad +\frac{1}{6} y_{,xxx}(x = \chi_2) \left(\frac{h}{2}\right)^3. \end{aligned} \tag{4.133}$$

When these expressions are substituted into equation (4.131), the first and third terms cancel, leaving

$$(y_{,x})^{(\mathrm{c.d.})}_{i+1/2} = (y_{,x})_{i+1/2} + \frac{1}{58} \left(y_{,xxx}(x = \chi_2) + y_{,xxx}(x = \chi_1)\right) h^2, \tag{4.134}$$

thus proving that the local error is of second order in h. So the approximation to y_{i+1} given by the central difference method is second order accurate, since

$$y_{i+1} = y_i + h \left(y^{(\mathrm{c.d.})}_{,x}\right)_{i+1/2} + \frac{1}{58} \left(y_{,xxx}(x = \chi_2) + y_{,xxx}(x = \chi_1)\right) h^3. \tag{4.135}$$

However, since the hydrodynamic equations presently studied are a complex system of several partial differential equations, it is somewhat difficult to predict the order of the global error. The derivatives with respect to the radial coordinate A and the null coordinate u appearing on the right hand sides of equations (4.47) to (4.53) introduce errors of the order ΔA^2 and Δu^2. In addition, the global error will always be larger than the local one. Assuming an integration over a fixed interval, the number of steps will increase as the stepwidth h decreases, thus lowering the order of the global error.

Let q be the correct value of some quantity at some final time and q_1 the approximation calculated using a stepwidth of h, q_2 the approximation using a stepwidth of $h/2$, and q_4 the approximation using a stepwidth $h/4$. If the

global error is of order k, the approximations are related to the exact result via

$$q_1 = q + \eta h^k, \tag{4.136}$$

$$q_2 = q + \eta \left(\frac{h}{2}\right)^k, \tag{4.137}$$

and

$$q_4 = q + \eta \left(\frac{h}{4}\right)^k, \tag{4.138}$$

where η is some constant. Calculating the ratio

$$\Lambda = \frac{q_1 - q_4}{q_1 - q_2} \tag{4.139}$$

the exact value q and the constant η cancel and one obtains the order of the global error

$$k = -\frac{\ln(\Lambda - 1)}{\ln(2)}. \tag{4.140}$$

To determine the order of the global error, the simulation was run with a constant stepwidth Δu until a certain u-value was reached and the values of several hydrodynamic quantities at arbitrary gridpoints were saved. Then the simulation was run again with a constant stepwidth $\Delta u/2$ and then again with $\Delta u/4$. Calculating the ratio Λ for all the quantities yielded values around

$$\Lambda \approx 1.5, \tag{4.141}$$

giving $k \approx 1$. The same procedure was executed with a constant stepwidth Δu and different radial steps ΔA, $\Delta A/2$, and $\Delta A/4$. The resultant order in this case was also $k \approx 1$. Thus we expect the hydrodynamic evolution scheme's global error to be **first order in space and time**.

5 Evolution of Electromagnetic Fields

5.1 Evolution Equations

In this section, an electromagnetic field is added to the scenario of a collapsing star. This makes it necessary to consider not only the stellar interior but also the vacuum exterior. And in addition to the equations of the hydrodynamic evolution, the Maxwell equations have to be solved.

In this work, we assume that the magnetic field strength is small, so that its influence on the spacetime and the motion of the fluid is negligible, i.e. the energy equation (3.34) and the Euler equation (3.35) are used without the additional terms of equations (3.56) and (3.58). Thus, the evolution of the spacetime and the fluid are completely the same as in the case without the electromagnetic field.

5.1.1 Interior

To obtain specific expressions for the electric and magnetic fields in the stellar interior, a (3+1)-foliation using comoving Misner-Sharp coordinates (cf. equation (4.1)) is assumed. Furthermore, the fluid is taken to be perfectly conducting, making it possible to use the equations of ideal MHD.

Using the fluid 4-velocity in Misner-Sharp coordinates

$$[u^\mu] = \left(e^{-\phi}, 0, 0, 0\right) \tag{5.1}$$

in the ideal MHD relation (3.52) yields

$$E^i = 0, \tag{5.2}$$

so the electric field corresponding to the Misner-Sharp foliation vanishes in the stellar interior under the assumption of ideal MHD.

Substituting $v^i = 0$ into the ideal MHD version of Faraday's law, equation (3.53), yields

$$\mathcal{B}^i_{,t} = 0, \tag{5.3}$$

which with the Misner-Sharp expression for γ becomes

$$\left(e^{\lambda/2} R^2 \sin\theta B^i\right)_{,t} = 0. \tag{5.4}$$

To transform the t-derivative into a derivative with respect to the Hernandez-Misner coordinate u, which is used in the hydrodynamical evolution scheme, one can again use relation (4.38), which leads to

$$\left(\frac{B^i}{\rho_0}\right)_{,u} = 0, \tag{5.5}$$

where equation (4.25) was also used. This can be integrated, yielding

$$\frac{B^i(u)}{B^i(u=0)} = \frac{\rho_0(u)}{\rho_0(u=0)}. \tag{5.6}$$

More meaningful than the components B^i of the vector $[B^i]$ with respect to the basis vectors e_i are the components $B^{\hat{i}}$ with respect to the normalized basis vectors

$$\hat{e}_i = \left(g^{ii}\right)^{1/2} e_i. \tag{5.7}$$

It follows from (5.7) that

$$B^{\hat{i}} = (g_{ii})^{1/2}\, B^i. \tag{5.8}$$

Inserting the metric components in Misner-Sharp coordinates into equation (5.6) and using equation (4.25) once more, one gets

$$\frac{B^{\hat{A}}(u)}{B^{\hat{A}}(0)} = \frac{R^2(0)}{R^2(u)} \tag{5.9}$$

and

$$\frac{B^{\hat{\theta}}(u)}{B^{\hat{\theta}}(0)} = \frac{B^{\hat{\varphi}}(u)}{B^{\hat{\varphi}}(0)} = \frac{\rho_0(u)R(u)}{\rho_0(0)R(0)}. \tag{5.10}$$

These relations immediately provide the magnetic field components in the stellar interior once the evolution of the hydrodynamical quantities R and ρ_0 is known and the initial magnetic field components are given.

5.1.2 Exterior

In the exterior region, the full Maxwell equations as given in (3.45) and (3.46) have to be evolved. A suitable (3+1)-foliation for this is given by Schwarzschild coordinates (4.77), for which the lapse function is

$$\alpha_{\mathrm{Schw}} = \left(1 - \frac{2M}{R}\right)^{1/2}, \tag{5.11}$$

the shift vector vanishes

$$\beta^i_{\mathrm{Schw}} = 0, \tag{5.12}$$

the determinant of the 3-dimensional metric on the spatial slices is

$$\gamma_{\mathrm{Schw}} = \left(1 - \frac{2M}{R}\right)^{-1} R^4 \sin^2\theta \tag{5.13}$$

and the extrinsic curvature is zero

$$K^{\mathrm{Schw}}_{ij} = 0. \tag{5.14}$$

Since there are no electric charges in the exterior of the star, the source-free Coulomb gauge

$$\Phi = 0 \tag{5.15}$$

can be used. Substituting all this into equations (3.45) and (3.46), they become

$$A_{i,t} = -\alpha E_i \tag{5.16}$$

and

$$E^i_{,t} = \sum_{j=1}^{3} \gamma^{-1/2} \left(\alpha \gamma^{1/2} \gamma^{ii} \gamma^{jj} \left(A_{j,i} - A_{i,j} \right) \right)_{,j}. \tag{5.17}$$

From now on, an axisymmetric solution shall be assumed, where E^φ and A_φ are the only nonzero components and all quantities are independent of the φ-coordinate. Under this assumption, the two evolution equations become

$$A_{\varphi,t} = -\left(1 - \frac{2M}{R}\right)^{1/2} E_\varphi \tag{5.18}$$

and

$$\begin{aligned} E^\varphi_{,t} \;=\; & -\left(1 - \frac{2M}{R}\right)^{1/2} \frac{1}{R^2 \sin\theta} \\ & \left(\left(\frac{1 - \frac{2M}{R}}{\sin\theta} A_{\varphi,R} \right)_{,R} + \left(\frac{1}{R^2 \sin\theta} A_{\varphi,\theta} \right)_{,\theta} \right). \end{aligned} \tag{5.19}$$

The fields E^φ and A_φ are now decomposed as in reference [2] according to

$$A_\varphi(t, R, \theta) = -\sum_l a^{(l)}(t, R) \left(1 - \mu^2\right) \frac{dP_l(\mu)}{d\mu} \tag{5.20}$$

and

$$E^\varphi(t, R, \theta) = \sum_l \frac{e^{(l)}(t, R)}{R^2} \frac{dP_l(\mu)}{d\mu}, \tag{5.21}$$

where $\mu = \cos\theta$ and P_l are the Legendre polynomials. Inserting these expressions gives an evolution equation for every component $a^{(l)}$ and $e^{(l)}$, namely

$$a^{(l)}_{,t} = \left(1 - \frac{2M}{R}\right)^{1/2} e^{(l)} \tag{5.22}$$

and

$$e^{(l)}_{,t} = \left(1 - \frac{2M}{R}\right)^{1/2} \left(\frac{2M}{R^2} a^{(l)}_{,R} + \left(1 - \frac{2M}{R}\right) a^{(l)}_{,RR} - \frac{l\,(l+1)}{R^2} a^{(l)} \right), \tag{5.23}$$

where the property of the Legendre polynomials

$$\left(\left(1 - \mu^2\right) \frac{dP_l(\mu)}{d\mu} \right)_{,\mu} = -l\,(l+1)\, P_l(\mu) \tag{5.24}$$

has been used. This shows that the different multipoles evolve completely independent from each other and the assumption of a pure dipole field ($l = 1$)

that will later be made is in fact consistent. Furthermore, differentiating equation (5.22) with respect to t yields

$$\begin{aligned} a^{(l)}_{,tt} &= \left(1-\frac{2M}{R}\right)^{1/2} e^{(l)}_{,t} \\ &= \left(1-\frac{2M}{R}\right)\left(\frac{2M}{R^2}a^{(l)}_{,R}+\left(1-\frac{2M}{R}\right)a^{(l)}_{,RR}-\frac{l\,(l+1)}{R^2}a^{(l)}\right). \end{aligned} \tag{5.25}$$

To simplify this equation, the two null coordinates

$$u = t - R - 2M\ln\left(\frac{R}{2M}-1\right) \tag{5.26}$$

and

$$v = t + R + 2M\ln\left(\frac{R}{2M}-1\right) \tag{5.27}$$

are introduced, with which the line element becomes

$$ds^2 = -\left(1-\frac{2M}{R}\right)dvdu + R^2d\theta^2 + R^2\sin^2\theta d\varphi^2. \tag{5.28}$$

In equation (5.25), the derivatives can be transformed by using the relations

$$\left.\frac{\partial}{\partial t}\right|_R = \left.\frac{\partial u}{\partial t}\right|_R \left.\frac{\partial}{\partial u}\right|_v + \left.\frac{\partial v}{\partial t}\right|_R \left.\frac{\partial}{\partial v}\right|_u = \left.\frac{\partial}{\partial v}\right|_u + \left.\frac{\partial}{\partial u}\right|_v \tag{5.29}$$

and

$$\left.\frac{\partial}{\partial R}\right|_t = \left.\frac{\partial u}{\partial R}\right|_t \left.\frac{\partial}{\partial u}\right|_v + \left.\frac{\partial v}{\partial R}\right|_t \left.\frac{\partial}{\partial v}\right|_u = \left(1-\frac{2M}{R}\right)^{-1}\left(\left.\frac{\partial}{\partial v}\right|_u - \left.\frac{\partial}{\partial u}\right|_v\right). \tag{5.30}$$

Ultimately, equation (5.25) becomes a wave equation in the form

$$2a^{(l)}_{,vu} + \frac{\left(1-\frac{2M}{R}\right)}{R^2}a^{(l)} = 0. \tag{5.31}$$

So in the end, with the symmetry assumptions made and the neglect of any backreaction from the electromagnetic field, the problem reduces to the evolution of one field $a^{(l)}$ in (1+1) dimensions.

5.2 Boundary Conditions

At the stellar surface, the electromagnetic fields in the exterior and interior regions have to be matched to each other. In a frame that is comoving with the surface, the orthogonal component of the B-field and the tangential component of the E-field have to be continuous across the boundary. Denoting field components measured in the comoving frame with a prime $'$, these conditions read

$$B^{\hat{A}'}_{(\mathrm{int})} = B^{\hat{R}'}_{(\mathrm{ext})} \tag{5.32}$$

and

$$E^{\hat{\varphi}'}_{(\mathrm{int})} = E^{\hat{\varphi}'}_{(\mathrm{ext})}. \tag{5.33}$$

The Misner-Sharp coordinates used in the stellar interior in the above section are already comoving, so

$$B^{\hat{A}'}_{(\mathrm{int})} = B^{\hat{A}}_{(\mathrm{int})} \tag{5.34}$$

and

$$E^{\hat{\varphi}'}_{(\mathrm{int})} = E^{\hat{\varphi}}_{(\mathrm{int})} = 0. \tag{5.35}$$

The Schwarzschild coordinates used in the exterior region on the other hand are not comoving with the stellar surface, so the field components $B^{\hat{R}'}$ and $E^{\hat{\varphi}'}$ as measured by a comoving observer u^μ have to be expressed in terms of the field components $B^{\hat{i}}$ and $E^{\hat{i}}$ as measured by an observer n^μ who is moving normal to the spatial slices defined by $t = \mathrm{const}$. The relations between these two types of components are given by

$$B^{\hat{R}'} = B^{\hat{R}} \tag{5.36}$$

and

$$E^{\hat{\varphi}'} = \Upsilon \left(E^{\hat{\varphi}} - \bar{v} B^{\hat{\theta}} \right), \tag{5.37}$$

where $\bar{v}$ and Υ are the velocity and gamma-factor associated with a Lorentz-boost from the frame of the comoving observer to the frame of the normal observer given by

$$\Upsilon = -u^\mu n_\mu = \left(1 - \bar{v}^2\right)^{-1/2} \tag{5.38}$$

(cf. [2]). With these results, the continuity conditions become

$$B^{\hat{A}}_{(\mathrm{int})} = B^{\hat{R}}_{(\mathrm{ext})} \tag{5.39}$$

and

$$E^{\hat{\varphi}}_{(\mathrm{ext})} = \bar{v} B^{\hat{\theta}}_{(\mathrm{ext})}. \tag{5.40}$$

Expressing $B^{\hat{R}}_{(\mathrm{ext})}$ in terms of A_φ according to equations (3.44) and (5.8) and using the decomposition (5.20), the condition (5.39) becomes

$$\begin{aligned} B^{\hat{A}}_{(\mathrm{int})} &= B^{\hat{R}}_{(\mathrm{ext})} \\ &= \frac{1}{R^2 \sin\theta} A_{\varphi,\theta} \\ &= \frac{1}{R^2 \sin\theta} \frac{d\mu}{d\theta} A_{\varphi,\mu} \\ &= \frac{1}{R^2} \sum_l a^{(l)} \left(-2\mu \frac{dP_l(\mu)}{d\mu} + \left(1 - \mu^2\right) \frac{d^2 P_l(\mu)}{d\mu^2} \right). \end{aligned} \tag{5.41}$$

Assuming a pure dipole field

$$a^{(l)} = \begin{cases} a & \text{if } l = 1 \\ 0 & \text{else} \end{cases} \tag{5.42}$$

in the exterior, the equation can be solved for a, yielding

$$a = -\frac{R^2 B^{\hat{A}}_{(\mathrm{int})}}{2\cos\theta}. \tag{5.43}$$

In order to reduce the other continuity condition (5.40) to a relation between the fields $e^{(l)}$ and $a^{(l)}$, the components $E^{\hat{\varphi}}_{(\mathrm{ext})}$ and $B^{\hat{\theta}}_{(\mathrm{ext})}$ are expanded likewise,

$$E^{\hat{\varphi}}_{(\mathrm{ext})} = R\sin\theta E^{\varphi}_{(\mathrm{ext})} = \sum_l \frac{e^{(l)}\sin\theta}{R}\frac{dP_l(\mu)}{d\mu}, \tag{5.44}$$

$$B^{\hat{\theta}}_{(\mathrm{ext})} = -\frac{1-\frac{2M}{R}}{R\sin\theta}A_{\varphi,R} = \frac{1-\frac{2M}{R}}{R\sin\theta}\sum_l a^{(l)}_{,R}\left(1-\mu^2\right)\frac{dP_l(\mu)}{d\mu}, \tag{5.45}$$

thus making (5.40) read

$$\begin{aligned}
&\sum_l \frac{e^{(l)}\sin\theta}{R}\frac{dP_l(\mu)}{d\mu} = \bar{v}\frac{1-\frac{2M}{R}}{R\sin\theta}\sum_l a^{(l)}_{,R}\left(1-\mu^2\right)\frac{dP_l(\mu)}{d\mu} \\
\Leftrightarrow \quad &\sum_l e^{(l)}\left(1-\mu^2\right)\frac{dP_l(\mu)}{d\mu} = \bar{v}\left(1-\frac{2M}{R}\right) \\
&\qquad\qquad \times\sum_l a^{(l)}_{,R}\left(1-\mu^2\right)\frac{dP_l(\mu)}{d\mu} \\
\Leftrightarrow \quad &e^{(l)} = \bar{v}\left(1-\frac{2M}{R}\right)a^{(l)}_{,R}.
\end{aligned} \tag{5.46}$$

In this relation, the velocity $\bar{v}$ remains to be determined. The normal observer in Schwarzschild coordinates is

$$[n_\mu] = (-\alpha,0,0,0) = \left(-\left(1-\frac{2M}{R}\right)^{1/2},0,0,0\right), \tag{5.47}$$

while the zeroth component of the comoving observer's 4-velocity follows from the line element in Schwarzschild coordinates (4.77) as

$$u^0 = \frac{dt}{d\tau} = \left(\left(1-\frac{2M}{R}\right)^{-2}\left(\frac{dR}{d\tau}\right)^2 + \left(1-\frac{2M}{R}\right)^{-1}\right)^{1/2}. \tag{5.48}$$

Using the relation

$$\frac{dR}{d\tau} = \frac{dR}{dx^\mu}\frac{dx^\mu}{d\tau} = u^\mu R_{,\mu} = U, \tag{5.49}$$

u^0 is rewritten as

$$u^0 = \left(\left(1-\frac{2M}{R}\right)^{-2}U^2 + \left(1-\frac{2M}{R}\right)^{-1}\right)^{1/2}. \tag{5.50}$$

Thus, the gamma-factor of the Lorentz-boost between the normal and comoving observers is given by

$$\Upsilon = -u^\mu n_\mu = \left(\left(1 - \frac{2M}{R}\right)^{-1} U^2 + 1\right)^{1/2} \tag{5.51}$$

and the corresponding velocity is

$$\bar{v} = \left(1 - \Upsilon^{-2}\right)^{1/2} = \left(1 - \left(\left(1 - \frac{2M}{R}\right)^{-1} U^2 + 1\right)^{-1}\right)^{1/2}. \tag{5.52}$$

So finally the continuity condition for the tangential component of the electric field at the stellar surface reads

$$e^{(l)} = \left(1 - \frac{2M}{R}\right)\left(1 - \frac{1}{\left(1 - \frac{2M}{R}\right)^{-1} U^2 + 1}\right)^{1/2} a^{(l)}_{,R}. \tag{5.53}$$

5.3 Initial Field Configuration

In this work, we consider an initial magnetic field configuration that is as homogeneous as possible in the stellar interior and matched to a pure dipole field in the exterior.

5.3.1 Interior

The interior field needs to satisfy the divergence equation

$$D_i B^i = \gamma^{-1/2}\left(\gamma^{1/2} B^i\right)_{,i} = 0, \tag{5.54}$$

making it impossible to use the Newtonian solution of a homegeneously magnetized star

$$B^{\hat{A}} = B\cos\theta, \tag{5.55}$$

$$B^{\hat{\theta}} = -B\sin\theta, \tag{5.56}$$

where B is a constant. Nevertheless, the initial magnetic field should reduce to this solution in the Newtonian limit. In addition, the interior magnetic field component $B^{\hat{A}}$ should be proportional to $\cos\theta$ at the stellar surface, making it possible to satisfy the boundary condition (5.43), where a should not depend on θ.

Specifically in this work, the following initial field configuration is adopted:

$$B^{\hat{A}} = B\cos\theta\left(1 + \left(\frac{A}{R}\right)^2\right)\left(1 + \left(\frac{A_{\mathrm{surf}}}{R_{\mathrm{surf}}}\right)^2\right)^{-1} \tag{5.57}$$

and

$$B^{\hat{\theta}} = -B\sin\theta\left(\Gamma + 4\pi\rho_0 R A\right)\left(1 + \left(\frac{A_{\mathrm{surf}}}{R_{\mathrm{surf}}}\right)^2\right)^{-1}. \tag{5.58}$$

In fact, this configuration has zero divergence since

$$\begin{aligned}\left(\gamma^{1/2}B^i\right)_{,i} &= \left(e^{\lambda/2}R^2\sin\theta e^{-\lambda/2}B^{\hat{A}}\right)_{,A} + \left(e^{\lambda/2}R^2\sin\theta R^{-1}B^{\hat{\theta}}\right)_{,\theta} \\ &= \sin\theta\cos\theta B\left(1+\left(\frac{A_{\rm surf}}{R_{\rm surf}}\right)^2\right)^{-1} \\ &\quad \left(2RR_{,A}+2A-2e^{\lambda/2}R\left(\Gamma+4\pi\rho_0 RA\right)\right) \\ &= \sin\theta\cos\theta B\left(1+\left(\frac{A_{\rm surf}}{R_{\rm surf}}\right)^2\right)^{-1} \\ &\quad \left(2Re^{\lambda/2}\Gamma+2A-2Re^{\lambda/2}\Gamma-2A\right) \\ &= 0, \end{aligned} \tag{5.59}$$

where the definition of Γ (4.8) and equation (4.25) have been used. Additionally, in the Newtonian limit, where $\Gamma \approx 1$, $A \approx m$ and therefore $A/R \ll 1$ and $4\pi\rho_0 R^2 \approx m_{,R}$ and therefore $4\pi\rho_0 RA \approx m_{,R}A/R \ll 1$, the magnetic field configuration given by equations (5.57) and (5.58) reduces to the homogeneous solution as demanded. Furthermore, the radial component reduces to

$$B^{\hat{A}}\Big|_{\rm surf} = B\cos\theta \tag{5.60}$$

at the stellar surface, making the matching condition (5.43) especially simple.

5.3.2 Exterior

The electric field in the stellar exterior can be taken to be initially zero

$$E^{\hat{i}} = 0 = e^{(l)}. \tag{5.61}$$

This is a manifestation of the star having no electric charge. The dipole magnetic field in the stellar exterior was calculated analytically in reference [24] (cf. also [2]). The components are expressed as

$$B^{\hat{R}} = -\frac{6\mu_{\rm d}\cos\theta}{R^3}\left(\frac{R}{2M}\right)^2\left(\frac{R}{2M}\ln\left(1-\frac{2M}{R}\right)+\frac{M}{R}+1\right) \tag{5.62}$$

and

$$\begin{aligned} B^{\hat{\theta}} &= \frac{6\mu_{\rm d}\sin\theta}{R^3}\left(\frac{R}{2M}\right)^2 \\ &\quad \left(\frac{R}{2M}\left(1-\frac{2M}{R}\right)^{1/2}\ln\left(1-\frac{2M}{R}\right)+\frac{1-\frac{M}{R}}{1-\frac{2M}{R}}\right), \end{aligned} \tag{5.63}$$

where $\mu_{\rm d}$ is the magnetic dipole moment of the star, which can be determined via the continuity condition (5.32). The result is

$$\mu_{\rm d} = -B\frac{R_{\rm surf}^3}{6}\left(\frac{2M}{R_{\rm surf}}\right)^2\left(\frac{R_{\rm surf}}{2M}\ln\left(1-\frac{2M}{R_{\rm surf}}\right)+\frac{M}{R_{\rm surf}}+1\right)^{-1}. \tag{5.64}$$

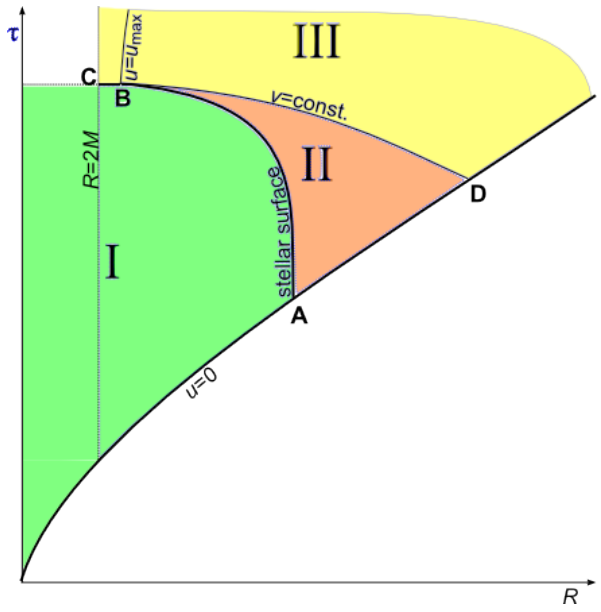

Figure 11: Computational domain for the evolution of the electromagnetic fields in the R-τ-plane. See text for details.

A vector potential A^i, which satisfies $B^i = \epsilon^{ijk} A_{k,j}$ for these magnetic field components, is given by

$$A_\varphi = -\frac{3\mu_\mathrm{d} \sin^2\theta}{2M} \left(\left(\frac{R}{2M} \right)^2 \ln\left(1 - \frac{2M}{R} \right) + \frac{R}{2M} + \frac{1}{2} \right). \tag{5.65}$$

Using the decomposition (5.20), this amounts to

$$a^{(l)} = \begin{cases} \frac{3\mu_\mathrm{d}}{2M} \left(\left(\frac{R}{2M} \right)^2 \ln\left(1 - \frac{2M}{R} \right) + \frac{R}{2M} + \frac{1}{2} \right) & \text{if } l = 1 \\ 0 & \text{else} \end{cases}. \tag{5.66}$$

At last, te only free parameter that remains in the initial field components (5.57), (5.58) and (5.66) is B, which is just a scaling parameter that can be chosen arbitrarily since the evolution equations are all linear.

5.4 Numerical Implementation

The computational domain can be divided into three distinct regions, as indicated in figures 11 and 12. Figure 11 depicts the evolution in the R-τ-plane and figure 12 shows the same situation in the v-u-plane. The initial data are used on the hypersurface defined by $u = 0$ (lower thick line in figure 11).

Region **I** is the stellar interior which is bounded by the initial hypersurface and the stellar surface evolving from its initial position at **A** until it passes the event horizon at **C**, which corresponds to $u = \infty$. However, the numerical

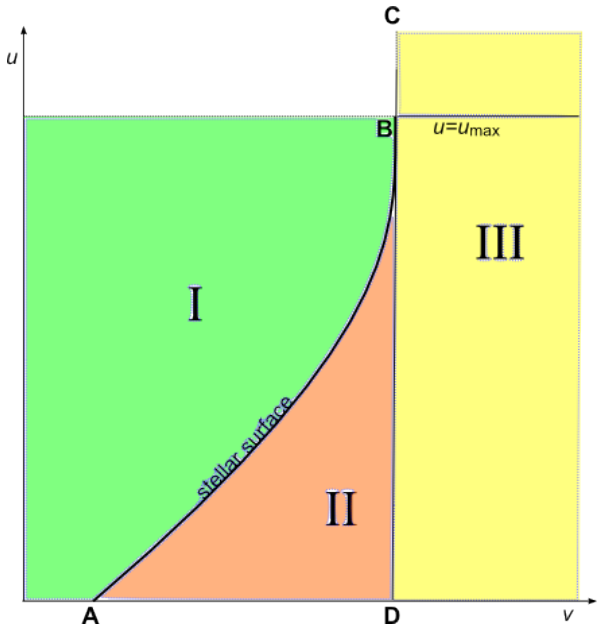

Figure 12: Computational domain for the evolution of the electromagnetic fields in the v-u-plane. The points **A**, **B**, **C** and **D** correspond to the same points in figure 11. The point **C** is located at $u = \infty$. See text for details.

evolution of the fluid is terminated, as mentioned before, as soon as the lapse function at the stellar surface becomes smaller than 10^{-3} at some finite value $u = u_{\max}$, which corresponds to **B** in the figures. In this region, the electric field remains absent due to the assumption of perfect conductivity and the magnetic field components are calculated directly from their initial values via equations (5.9) and (5.10) while the hydrodynamic evolution is conducted.

Regions **II** and **III** comprise the exterior of the star. As mentioned before, a pure dipole field ($l = 1$) is assumed there, making the decomposition (5.20) and (5.21)

$$A_\varphi = -a \sin^2 \theta \tag{5.67}$$

and

$$E^\varphi = \frac{e}{R^2}. \tag{5.68}$$

The field that is actually evolved is a, which immediately gives A_φ and thereby $B^{\hat{R}}$ and $B^{\hat{\theta}}$. E^φ is then also known, since e can be calculated from a via equation (5.22). As initial data, a as given in equation (5.66) is used on the $(u = 0)$-plane.

Region **II** is bounded by the stellar surface on the one side and the line of constant $v = v_{\mathbf{B}}$, i.e. the ingoing light ray that hits the stellar surface in the event where the hydrodynamical evolution is terminated, on the other side. Here, the field a is evolved simultaneously with the hydrodynamical evolution of the stellar interior. For each step Δu in region **I**, a step Δv is calculated

in region **II**, where we assume that $\Delta v = \Delta u$. The mixed derivative in the evolution equation (5.31) is expressed by finite differences and the equation is solved for a_{n+1}^{i+1}, yielding

$$\begin{aligned} a_{i+1}^{n+1} &= -\frac{(\Delta v)_{i+1/2}\,(\Delta u)^{n+1/2}}{2}\left(1-\frac{2M}{R_{i+1/2}^{n+1/2}}\right)\frac{a_{i+1/2}^{n+1/2}}{\left(R_{i+1/2}^{n+1/2}\right)^2} \\ &\quad + a_{n+1}^{i} + a_{n}^{i+1} - a_{n}^{i}. \end{aligned} \tag{5.69}$$

Here, n and i correspond to the discretized u- and v-coordinates. Approximating $a_{i+1/2}^{n+1/2} \widehat{=} a(v+\Delta v/2, u+\Delta u/2)$ by linear interpolation between $a(v+\Delta v, u)$ and $a(v, u+\Delta u)$, this equation allows the calculation of $a(v+\Delta v, u+\Delta u)$ from $a(v,u)$, $a(v+\Delta v, u)$ and $a(v, u+\Delta u)$. To this end, the circumferential radius R has to be calculated as a function of u and v. From the definitions of u and v, equations (5.26) and (5.27), follows

$$\frac{1}{2}(v-u) = R + 2M \ln\left(\frac{R}{2M} - 1\right), \tag{5.70}$$

which can be solved numerically for R. In every step Δv, this procedure is started at the $(u=0)$-side of region **II** (at the bottom of figure 12), where the values of a are determined by the initial data and carried out toward larger u up to the second-to-last gridpoint. For the last gridpoint there is no known value for $a(v, u+\Delta u)$, since the gridpoint $(v, u+\Delta u)$ is inside the star. But the boundary condition on the stellar surface provides another means to calculate the a-value on the last gridpoint which actually lies on the surface of the star. Inserting $B_{(\mathrm{int})}^{\hat{A}}$ from equation (5.9) into the boundary condition (5.43), the expression for the field a on the stellar surface becomes

$$a_{\mathrm{surf}} = -\frac{B_{(\mathrm{int})}^{\hat{A}}(u=0) R_{\mathrm{surf}}^2(u=0)}{2\cos\theta} \tag{5.71}$$

and it turns out that a_{surf} is actually constant. Inserting the expression (5.57) for $B_{(\mathrm{int})}^{\hat{A}}(u=0)$, it becomes

$$a_{\mathrm{surf}} = -\frac{1}{2} B R_{\mathrm{surf}}^2(u=0). \tag{5.72}$$

The scaling factor B is arbitrarily set to one in the simulations.

In this way, the field a is calculated in region **II** while the hydrodynamic evolution is conducted in region **I**. When the hydrodynamical evolution is terminated, the field a is known up to the v-coordinate of the point in which the stellar surface is at the moment of the termination (cf. figures 11 and 12).

The evolution of a in region **III**, which is bounded by the $(u=0)$-hypersurface, the event horizon at $u=\infty$ and the hypersurface defined by $v = v_{\mathbf{B}}$, is conducted afterwards. Before the evolution, the gridpoints are

redistributed in such a way that Δu is now constant on the ingoing light ray from **D** to **B**.

In order not to miss out on the region between the $(u = u_{\max})$-hypersurface and the event horizon (the left part of region **III** in figure 11 and the upper part of region **III** in figure 12), additional equally spaced gridpoints are added between the points **B** and **C** and they are assigned an a-value by linear extrapolation from the two gridpoints nearest to **B** on the $(v = v_{\mathbf{B}})$-line, according to the prescription

$$a_{i_{\max}}^{n_{\max}+x} = a_{i_{\max}}^{n_{\max}} + \frac{a_{i_{\max}}^{n_{\max}} - a_{i_{\max}}^{n_{\max}-1}}{R_{i_{\max}}^{n_{\max}} - R_{i_{\max}}^{n_{\max}-1}} \left(R_{i_{\max}}^{n_{\max}+x} - R_{i_{\max}}^{n_{\max}} \right), \tag{5.73}$$

where the point **B** corresponds to $(u_{\mathbf{B}}, v_{\mathbf{B}}) \widehat{=} (n_{\max}, i_{\max})$. This procedure follows references [9] and [23], where it was used for metric perturbations. The number of extra gridpoints is determined by the condition that the circumferential radius $R_{\min}$ of the new innermost gridpoint $\tilde{u}_{\max}$ after a certain Schwarzschild-time $t_{\max}$ is the same as the circumferential radius of the stellar surface at the moment of the termination of the hydrodynamical evolution $R(u_{\max}, v_{\mathbf{B}})$. The Schwarzschild-time at this gridpoint is determined directly from equations (5.26) and (5.27),

$$t_{\max} = \frac{1}{2} \left(\tilde{u}_{\max} + v(\tilde{u}_{\max}, t_{\max}) \right) \tag{5.74}$$

and the lines of constant R are the lines of constant $(v - u)$, yielding the condition

$$v(\tilde{u}_{\max}, t_{\max}) - \tilde{u}_{\max} = v_{\mathbf{B}} - u_{\max}. \tag{5.75}$$

Putting toghether the last two equations, one obtains

$$\tilde{u}_{\max} = t_{\max} - \frac{1}{2} \left(v_{\mathbf{B}} - u_{\max} \right). \tag{5.76}$$

After this extrapolation, the evolution of the field a is conducted in region **III** with $\Delta v = \Delta u = \text{const.}$, using the same scheme as in region **II**, only without the boundary condition at the stellar surface which is no longer needed.

5.5 Calculated Magnetic Fields

The result for the evolution of the field a is shown in figure 13 in the v-u-plane for the collapse of a stellar model with a polytropic equation of state. In the v-u-plane as shown here, lines of constant circumferential radius R correspond to lines from left to right, diagonally across the square section shown here. Lines of constant Schwarzschild time t correspond to diagonal lines from front to back. While the distance between two lines of constant $t = t_1$ and $t = t_1 + \Delta t$ is the same everywhere in the v-u-plane, this is not true for lines of constant $R = R_1$ and $R = R_1 + \Delta R$, i.e. these two lines would be further apart in the v-u-plane if R_1 is closer to the event horizon. So the region into which the a-values are extrapolated after the termination of the hydrodynamical evolution

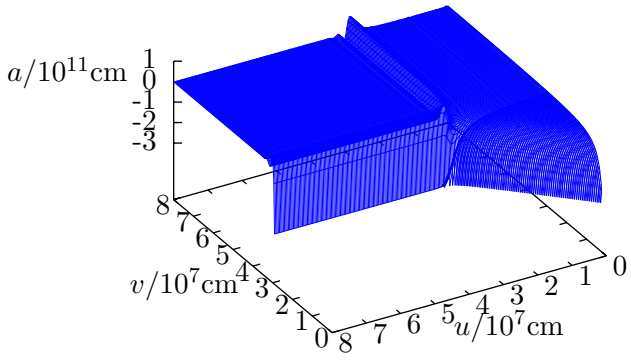

Figure 13: a-field in the v-u-plane for a collapsing polytropic star with $n = 1.5$, $K = 5.38 \cdot 10^9$ cm^{4}g$^{-2/3}$s^{-2} and a central density of $\rho_{0,\mathrm{centr}} = 5.0 \cdot 10^{15}$g cm^{-3}.

is in fact only very small in terms of differences of circumferential radii. In the case shown in figure 13, it has a width of $\Delta R < 0.002M$.

The stellar interior corresponds to the region in front of the colored surface in figure 13 (cf. also figures 11 and 12 for orientation). No values are shown in the interior, since a was only defined in the exterior. It can be seen that a is constant on the stellar surface and that the exterior field remains almost constant during the first slow phase of the collapse, during which the stellar surface is almost a line of constant R. When the collapse gathers momentum, a wave emerges and travels outward with the speed of light, i.e. along a line of constant u. It is followed by further oscillations parallel to it.

As shown in reference [26], the magnetic field lines in an axisymmetric configuration with no toroidal fluid flow are simply the lines of constant A_φ. Figures 14 and 15 show snapshots of the resulting field lines at selected Schwarzschild-times t, where the stellar surface is represented by the thick line. The initial field configuration is a simple dipole field which stays roughly unchanged during the first slow phase of the collapse until about $t \approx 650$. This corresponds to the phase during which the stellar surface resembles a straight line in figure 13. Only small ripples in the magnetic field lines caused by the slight wobbling of the surface can be seen in the middle panel of figure 14. In the lower panel of figure 14, the rapid phase of the collapse has just taken place and the wave that was already anticipated from figure 13 can be

seen very clearly. Figure 15 shows how the radiation from the collapse travels outward and leaves behind a region where the magnetic field has practically vanished.

The crucial part of the collapse for the formation of the outgoing electromagnetic wave is shown as a close-up in figures 16 and 17. In the upper panel of figure 16, the field lines are still similar to their initial state, although the star has already shrunk considerably. In the other two panels, they can be seen to be closing and figure 17 shows the formation of more wave crests as well as their motion away from the star.

5.6 Tests of the Numerical Scheme

In order to check our numerical code for the evolution of the magnetic field, we make three tests, i.e. the determination of the wavelength, the late-time behavior, and the energy conservation.

5.6.1 Wavelength of the Radiation

The wavelength of the outgoing radiation can be determined by looking at the a-field at a constant Schwarzschild-time. Figure 18 shows an example of such a snapshot at $t = 800M$. Measuring the distance of the wave crests yields a wavelength of approximately

$$\lambda \approx 25M. \tag{5.77}$$

This is in good agreement with the results in reference [6], where it is shown that

$$\omega = \frac{0.509}{2M}, \tag{5.78}$$

or $\lambda = 24.7M$ for electromagnetic dipole modes around a Schwarzschild black hole (cf. also [2]).

5.6.2 Late-Time Behavior

It was shown in reference [19] that an initially static multipole perturbation on a background describing a collapsing star will die out as $t^{-(2l+2)}$ and a multipole perturbation that develops during the collapse will die out as $t^{-(2l+3)}$. In this work, we focus on the case of $l = 1$ and the electromagnetic field, is static in the beginning, so one would expect it to die out as t^{-4} (cf. also [2]).

The non-vanishing electromagnetic field components can be calculated from the field a via

$$B^{\hat{R}} = -\frac{2a}{R^2}\sin\theta, \tag{5.79}$$

$$B^{\hat{\theta}} = \frac{1}{R}\sin\theta\left(1-\frac{2M}{R}\right)^{1/2} a_{,R} = \frac{\sin\theta}{R\left(1-\frac{2M}{R}\right)^{1/2}}\left(a_{,v}-a_{,u}\right), \tag{5.80}$$

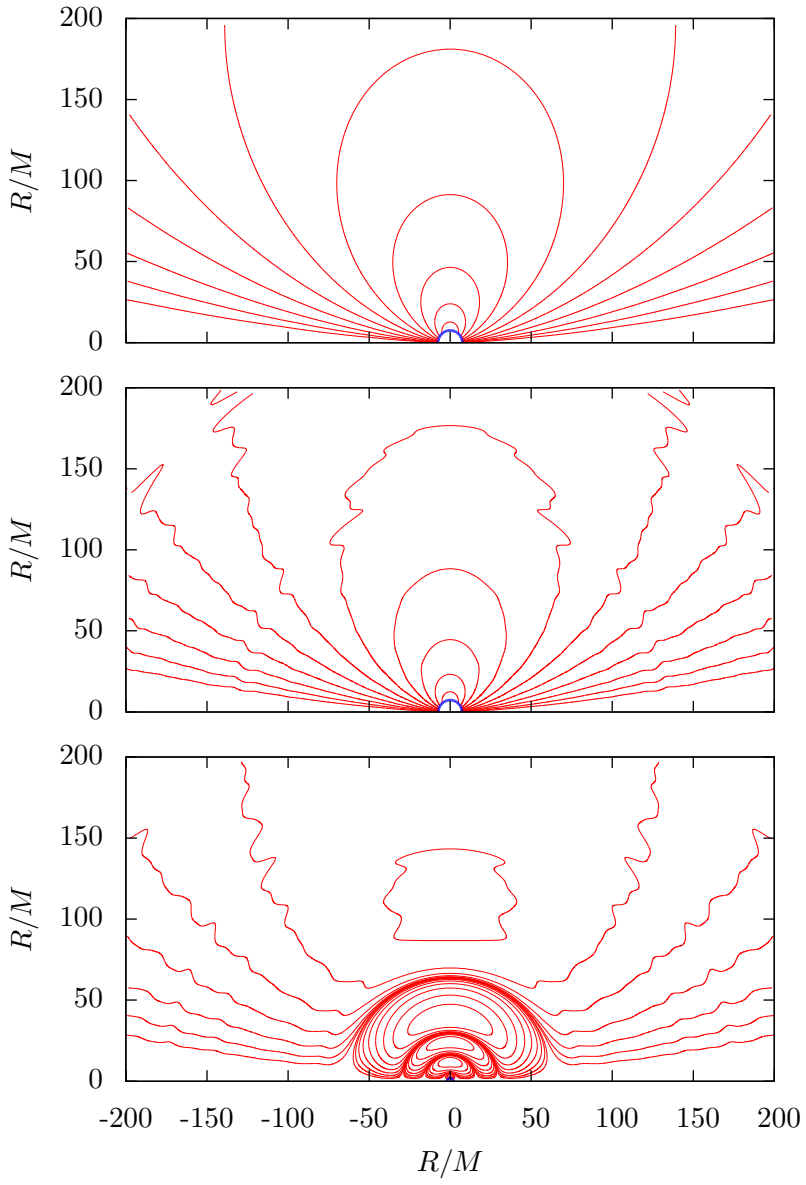

Figure 14: Magnetic field lines in the exterior of a collapsing polytrope with $n = 1.5$, $K = 5.38 \cdot 10^9$ cm^{4}g$^{-2/3}$s^{-2} and a central density of $\rho_{0,\mathrm{centr}} = 4.0 \cdot 10^{15}$ g cm^{-3} on a half-plane bisecting the star. The thick line denotes the stellar surface. The panels correspond to $t/M = 0,\ 350$, and 700 from top to bottom.

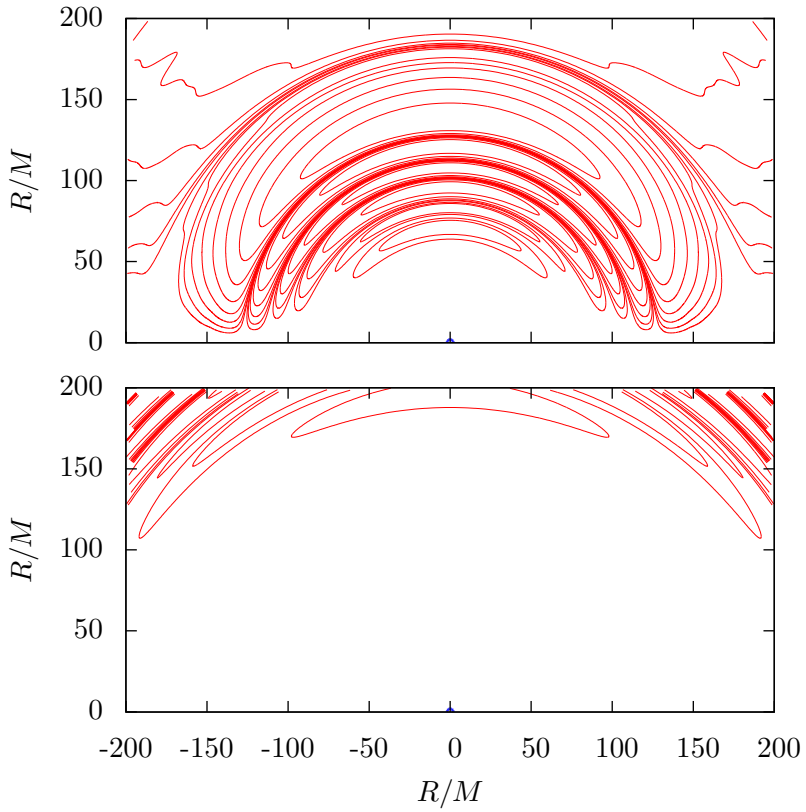

Figure 15: Same as figure 14. The panels correspond to $t/M = 800$ and 950 from top to bottom.

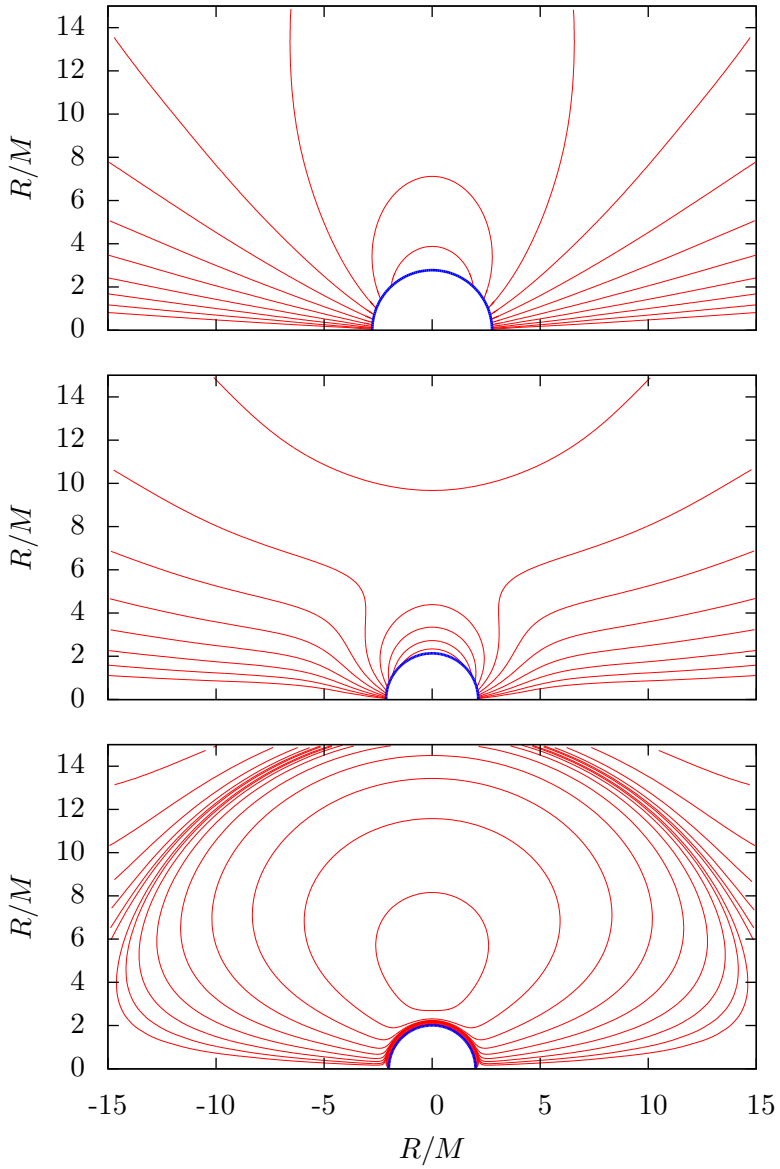

Figure 16: Close-up view of the situation depicted in figure 14 and 15. The panels correspond to $t/M = 655,\ 660$, and 665 from top to bottom.

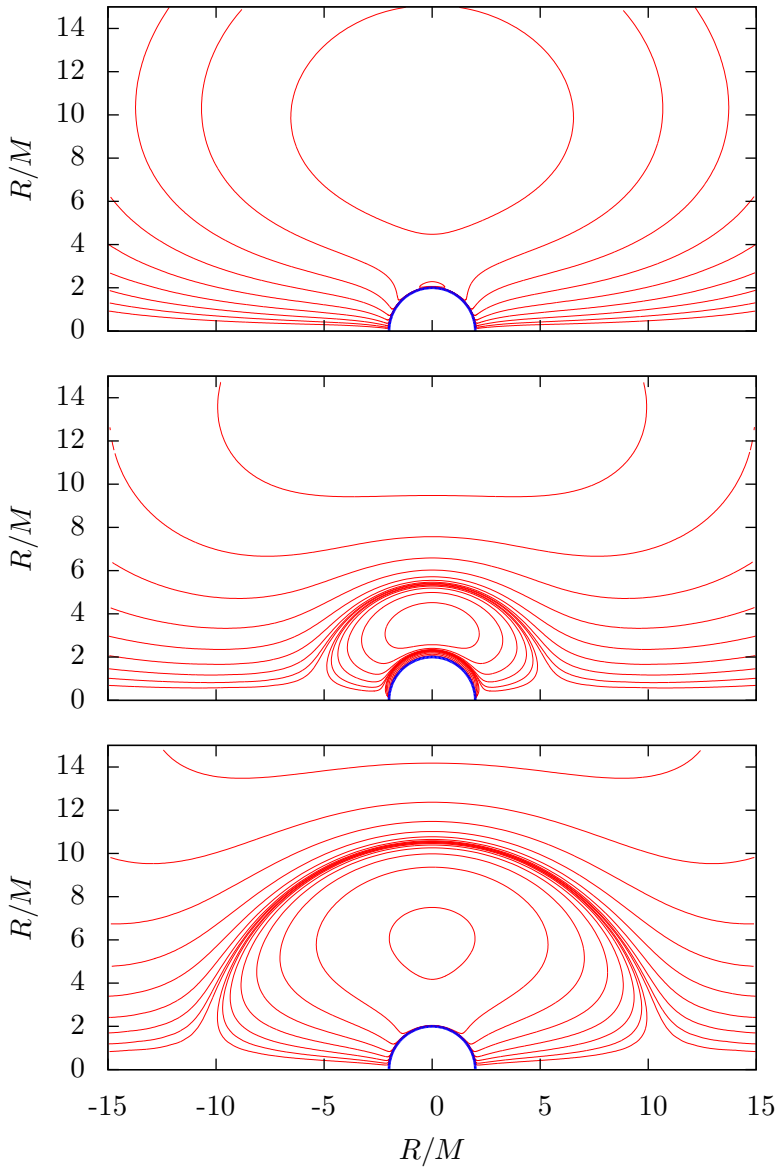

Figure 17: Same as figure 16. The panels correspond to $t/M = 670,\ 675$, and 680 from top to bottom.

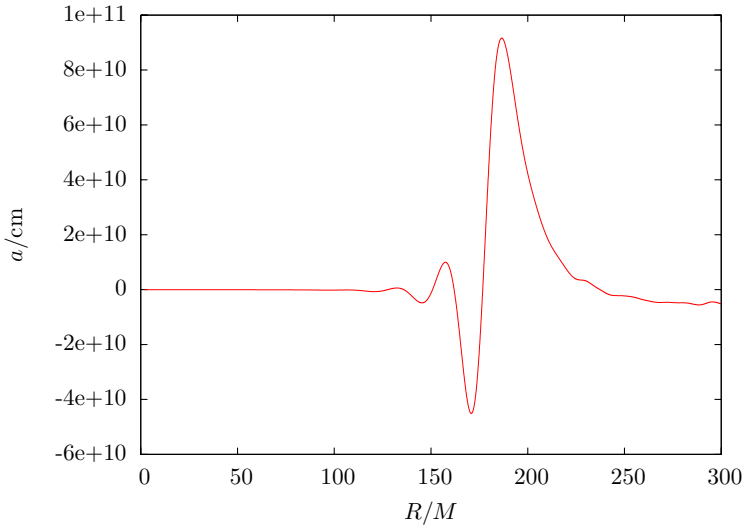

Figure 18: Field a in the stellar exterior at Schwarzschild-time $t/M = 800$ for a collapsing polytropic star with $n = 1.5$, $K = 5.38 \cdot 10^9$ cm^{4}g$^{-2/3}$s^{-2} and a central density of $\rho_{0,\mathrm{centr}} = 4.0 \cdot 10^{15}$ g cm^{-3}.

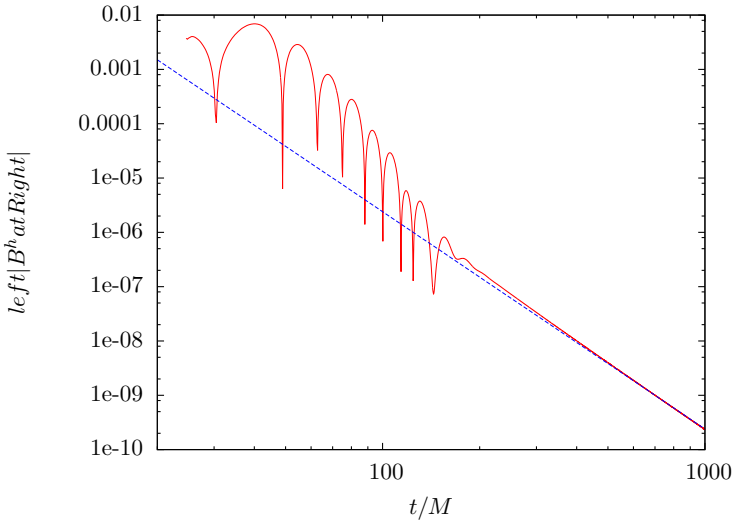

Figure 19: Time-dependence of $|B^{\hat{R}}|$ at $R = 20M$ and $\theta = \pi/4$ for a collapsing dust sphere with an initial ratio of circumferential surface radius to mass of $R_{0,\mathrm{surf}}/M = 4$. The dashed line corresponds to a fall-off proportional to t^{-4}.

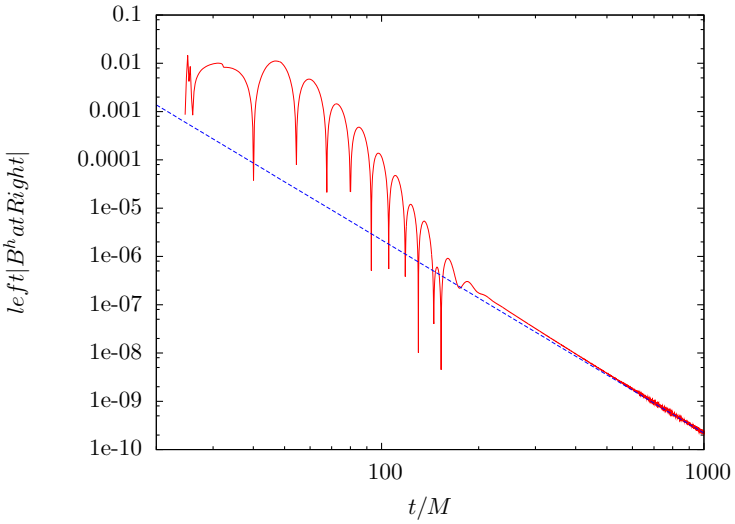

Figure 20: Time-dependence of $|B^{\hat{\theta}}|$ at $R = 20M$ and $\theta = \pi/4$ for a collapsing dust sphere with an initial ratio of circumferential surface radius to mass of $R_{0,\mathrm{surf}}/M = 4$. The dashed line corresponds to a fall-off proportional to t^{-4}.

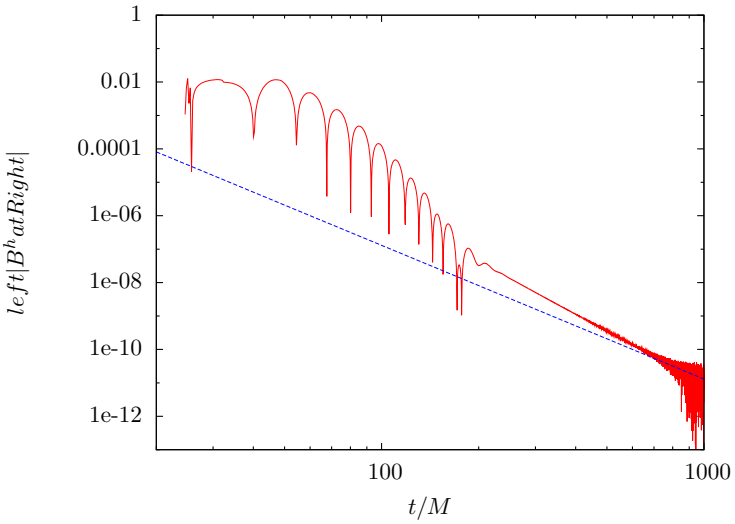

Figure 21: Time-dependence of $|E^{\hat{\varphi}}|$ at $R = 20M$ and $\theta = \pi/4$ for a collapsing dust sphere with an initial ratio of circumferential surface radius to mass of $R_{0,\mathrm{surf}}/M = 4$. The dashed line corresponds to a fall-off proportional to t^{-4}.

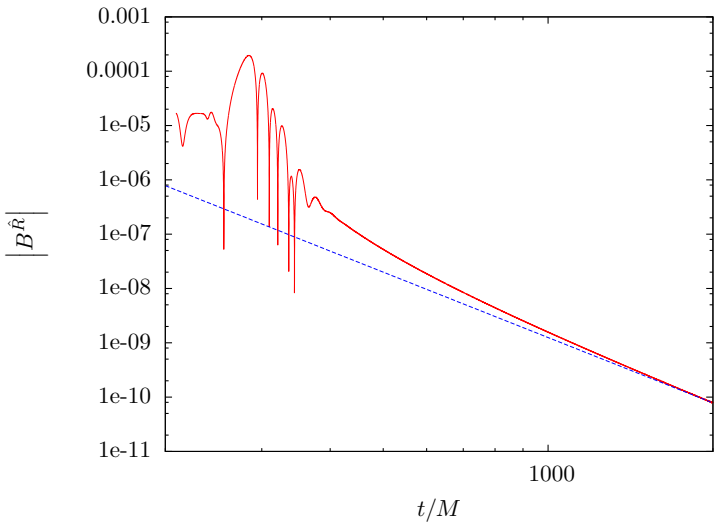

Figure 22: Time-dependence of $|B^{\hat{R}}|$ at $R = 200M$ and $\theta = \pi/4$ for a collapsing polytrope with $n = 1.5$, $K = 5.38 \cdot 10^9$ cm^{4}g$^{-2/3}$s^{-2} and a central density of $\rho_{0,\mathrm{centr}} = 60.0 \cdot 10^{15}$ g cm^{-3}. The dashed line corresponds to a fall-off proportional to t^{-4}.

and

$$E^{\hat{\varphi}} = \frac{1}{R}\sin\theta\left(1-\frac{2M}{R}\right)^{-1/2} a_{,t} = \frac{\sin\theta}{R\left(1-\frac{2M}{R}\right)^{1/2}}\left(a_{,v}+a_{,u}\right). \tag{5.81}$$

Figures 19 to 21 show the time-dependence of these field components for the case of Oppenheimer-Snyder collapse at an arbitrary point outside of the star. These graphs turn out to resemble closely the corresponding figures in reference [2]. They also show that the late-time behavior of the field components is as anticipated, although the high relative numerical errors for very small field strengths disturb the picture somewhat at very late times.

Similar pictures are presented for the collapse of a perfect fluid with polytropic equation of state in figures 22 to 24. The results in this case are also in accordance with a t^{-4} fall-off, but the asymptotic behavior is approached more slowly, which may give a higher importance to the numerical inaccuracies that can be seen in figures 23 and 24 and arise from the calculation of the derivatives in equations (5.80) and (5.81).

5.6.3 Energy Conservation

Following reference [2], one can derive an energy conservation law for the exterior region which can easily be checked numerically.

Since the Schwarzschild metric is independent of t, the vector field

$$\xi^\mu = \delta^\mu_0 \tag{5.82}$$

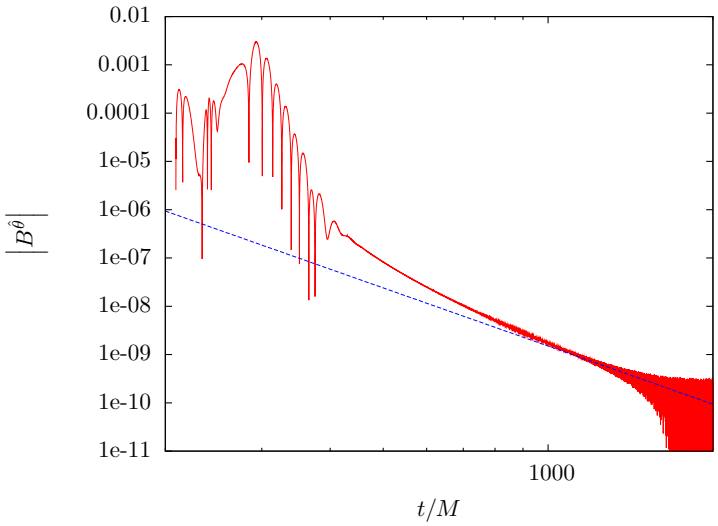

Figure 23: Time-dependence of $|B^{\hat{\theta}}|$ at $R = 200M$ and $\theta = \pi/4$ for a collapsing polytrope with $n = 1.5$, $K = 5.38 \cdot 10^9$ cm^{4}g$^{-2/3}$s^{-2} and a central density of $\rho_{0,\mathrm{centr}} = 60.0 \cdot 10^{15}$ g cm^{-3}. The dashed line corresponds to a fall-off proportional to t^{-4}.

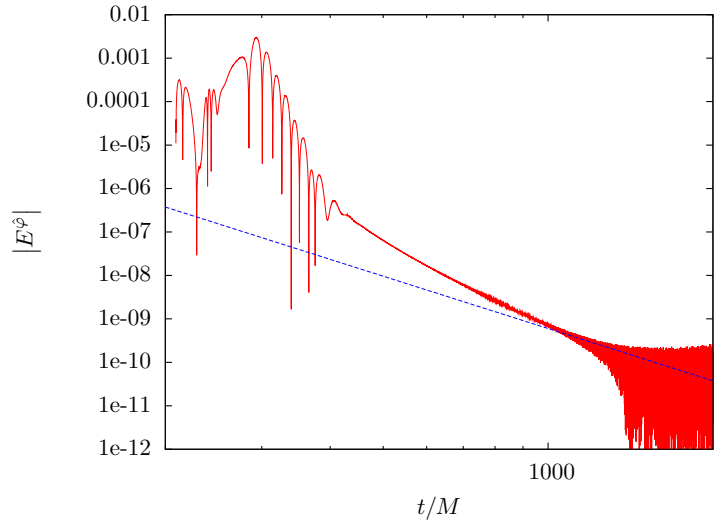

Figure 24: Time-dependence of $|E^{\hat{\varphi}}|$ at $R = 200M$ and $\theta = \pi/4$ for a collapsing polytrope with $n = 1.5$, $K = 5.38 \cdot 10^9$ cm^{4}g$^{-2/3}$s^{-2} and a central density of $\rho_{0,\mathrm{centr}} = 60.0 \cdot 10^{15}$ g cm^{-3}. The dashed line corresponds to a fall-off proportional to t^{-4}.

is a killing vector field, i.e.

$$\xi_{\nu;\mu} + \xi_{\mu;\nu} = 0. \tag{5.83}$$

Together with the symmetry of the energy-momentum tensor,

$$T^{\mu\nu} = T^{\nu\mu}, \tag{5.84}$$

and the vanishing of its divergence,

$$T^{\mu\nu}{}_{;\mu} = 0, \tag{5.85}$$

this yields

$$\begin{aligned} \left(T^{\mu\nu}\xi_\nu\right)_{;\mu} &= \xi_\nu T^{\mu\nu}{}_{;\mu} + T^{\mu\nu}\xi_{\nu;\mu} \\ &= -T^{\mu\nu}\xi_{\mu;\nu} \\ &= -T^{\mu\nu}\xi_{\nu;\mu} - \xi_\nu T^{\mu\nu}{}_{;\mu} \\ &= -\left(T^{\mu\nu}\xi_\nu\right)_{;\mu}. \end{aligned} \tag{5.86}$$

Therefore, the quantity

$$I^\mu = T^{\mu\nu}\xi_\nu \tag{5.87}$$

is corresponding to a conserved 4-current, i.e.

$$I^\mu_{;\mu} = 0. \tag{5.88}$$

Integrating this equation over a 4-volume V and transforming to a surface integral yields

$$\oint_{\partial V} I^\mu d^3\Sigma_\mu = 0. \tag{5.89}$$

Assuming that the 4-volume is bounded by two circumferential radii R_1 and R_2, as well as two Schwarzschild times t_1 and t_2, equation (5.89) can be written in the form

$$\mathcal{E}(t_2) - \mathcal{E}(t_1) + \mathcal{I}(R_2) - \mathcal{I}(R_1) = 0, \tag{5.90}$$

where

$$\mathcal{E}(t) = \int_{R_1}^{R_2} dR \int_0^\pi d\theta \int_0^{2\pi} d\varphi (-g)^{1/2}\, I^t \tag{5.91}$$

is the energy contained in the 3-volume bounded by R_1 and R_2 at the time t and

$$\mathcal{I}(R) = \int_{t_1}^{t_2} dt \int_0^\pi d\theta \int_0^{2\pi} d\varphi (-g)^{1/2}\, I^R \tag{5.92}$$

is the integrated energy flux across a sphere located at a circumferential radius R.

In our case, the determinant of the metric is given in Schwarzschild coordinates as

$$g = -R^4 \sin^2\theta \tag{5.93}$$

and the energy-momentum tensor is given by equation (3.55), since no matter is present in the stellar exterior. The Faraday tensor $F^{\mu\nu}$ is given in terms of the electric and magnetic field by equation (3.36). Using these expressions, the t-component of the conserved current becomes

$$\begin{aligned} I^t &= -\frac{1}{8\pi}\left(E_i E^i + B_i B^i\right) \\ &= -\frac{1}{8\pi}\left(\gamma^{\varphi\varphi}\left(E_\varphi\right)^2 + \gamma_{RR}\left(B^R\right)^2 + \gamma_{\theta\theta}\left(B^\theta\right)^2\right). \end{aligned} \tag{5.94}$$

Expressing B^R and B^θ in terms of A_φ and using the decompositions (5.67) and (5.68) yields

$$I^t = -\frac{1}{8\pi}\left(\frac{\sin^2\theta}{R^2}e^2 + \frac{4\cos^2\theta}{R^4}a^2 + \frac{\left(1-\frac{2M}{R}\right)\sin^2\theta}{R^2}\left(a_{,R}\right)^2\right). \tag{5.95}$$

After inserting this into equation (5.91), carrying out the angular integration, and expressing everything in terms of a and its derivatives with respect to u and v, the energy contained in the 3-volume finally becomes

$$\mathcal{E}(t) = -\frac{2}{3}\int_{R_1}^{R_2}\left(\left(1-\frac{2M}{R}\right)^{-1}\left(\left(a_{,v}\right)^2 + \left(a_{,u}\right)^2\right) + \frac{a^2}{R^2}\right)dR. \tag{5.96}$$

Following the same procedure, the R-component of the conserved current becomes

$$I^R = \sin^2\theta\frac{\left(1-\frac{2m}{R}\right)^{3/2}}{4\pi R^2}ea_{,R} \tag{5.97}$$

and the integrated energy flux

$$\mathcal{I}(R) = \frac{2}{3}\int_{t_1}^{t_2}\left(\left(a_{,v}\right)^2 - \left(a_{,u}\right)^2\right)dt. \tag{5.98}$$

Equations (5.96) and (5.98) make it possible to calculate $\mathcal{E}$ and $\mathcal{I}$ numerically at any given Schwarzschild time t. With these expressions, a quantity

$$\bar{\mathcal{E}}(t) = \frac{\mathcal{E}(t) + \mathcal{I}(R_2) - \mathcal{I}(R_1)}{\mathcal{E}(t=0)} = 1 \tag{5.99}$$

can be calculated, which should be constantly equal to one according to equation (5.90).

The corresponding result is shown in figure 25, where an inner boundary R_1 of 1.02 times the initial circumferential radius of the stellar surface and an outer boundary of $R_2 = 300M$ were chosen. In the figure, the sign of the energy flux across the inner boundary is changed in order to make all quantities positive. Thus, the thick curve is the sum of all the other curves. This graph shows that the condition for the conservation of energy, equation (5.99) is satisfied with an accuracy better than 2%. It can also be seen that about 75% of the electromagnetic energy that is initially stored in the observed region will flow inward into the emerging black hole and only about 25% of it will flow outward in the form of the observed electromagnetic wave.

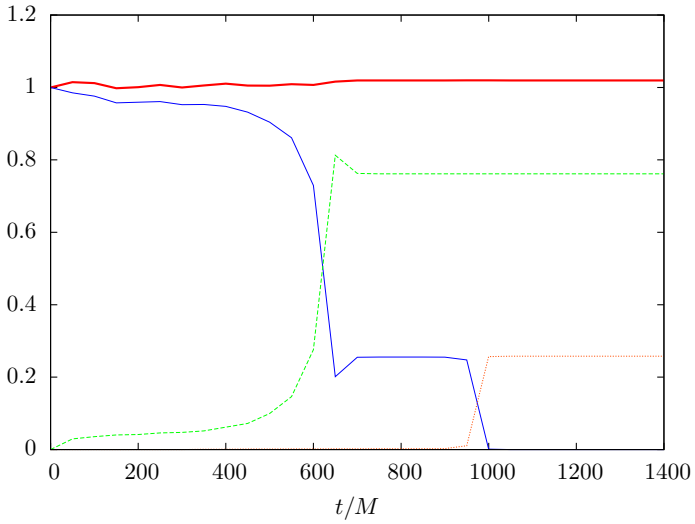

Figure 25: Energy balance of the 3-volume bounded by $R_1 = 1.02R_{0,\mathrm{surf}}$ and $R_2 = 300M$ for the collapse of a polytrope with $n = 1.5$, $K = 5.38 \cdot 10^9$ cm^{4}g$^{-2/3}$s^{-2} and a central density of $\rho_{0,\mathrm{centr}} = 4.0 \cdot 10^{15}$ g cm^{-3}. The solid line depicts the normalized energy $\mathcal{E}(t)/\mathcal{E}(t=0)$ contained within the volume, the dashed line the normalized integrated energy flux across the inner boundary $-\mathcal{I}(R_1)/\mathcal{E}(t=0)$, the dotted line the normalized integrated energy flux across the outer boundary $\mathcal{I}(R_2)/\mathcal{E}(t=0)$, and the thick line the quantity $\bar{\mathcal{E}}(t)$ defined in the text.

6 Collapse to a Neutron Star

In this section, we consider a different scenario from the above, in which the collapsing star does not necessarily form a black hole. The collapse can be obstructed by a stiffening of the equation of state at high densities so that a star that is initially in hydrostatic equilibrium will form a more compact star after the collapse. This is motivated for example by the scenario of an iron core of a massive star collapsing to a proto neutron star triggering a supernova explosion.

6.1 Equation of State

The previously used single polytrope is changed in such a way that the equation of state is now composed of two different polytropic equations of state for different density regimes,

$$P = \begin{cases} K_1 \rho_0^{\gamma_1} & \text{for } \rho_0 < \rho_{0,\text{crit}} \\ K_2 \rho_0^{\gamma_2} & \text{for } \rho_0 \geq \rho_{0,\text{crit}} \end{cases} . \tag{6.1}$$

The γ-values are chosen such that

$$\gamma_2 > \gamma_1, \tag{6.2}$$

so the equation of state is stiffer for densities above some critical density ρ_0, which will be chosen to have the same order of magnitude as the nuclear density.

In order for the equation of state to be continuous at the critical density, the relation

$$K_1 \rho_{0,\text{crit}}^{\gamma_1} = K_2 \rho_{0,\text{crit}}^{\gamma_2} \tag{6.3}$$

has to hold. So the polytropic constant K_1 is determined as a function of the polytropic constant K_2 and the critical rest-mass density $\rho_{0,\text{crit}}$ according to

$$K_1 = K_2 \rho_{0,\text{crit}}^{\gamma_2 - \gamma_1}. \tag{6.4}$$

Integrating the Oppenheimer-Volkoff equation as given in (4.126) and (4.127) for a number of different central densities $\rho_{0,\text{centr}}$ leads to the graph shown in Figure 26, where we adopt the parameter values as $\gamma_1 = 4/3$, $\gamma_2 = 2$, $K_2 = 100$ km^2, and $\rho_{0,\text{crit}} = 4.0 \times 10^{-14}$ cm^{-2}. Models on the declining branches on the right and the very left of the panel are expected to be radially unstable, whereas models on the rising branch between the local mass minimum and the local mass maximum should be stable.

6.2 Numerical Results

The new scenario does not call for any change in the code except the adaptation to the new equation of state (6.1). In order to force the star to collapse rather than expand from its unstable initial state, the pressure is reduced by a few percent throughout the whole star for the very first timestep.

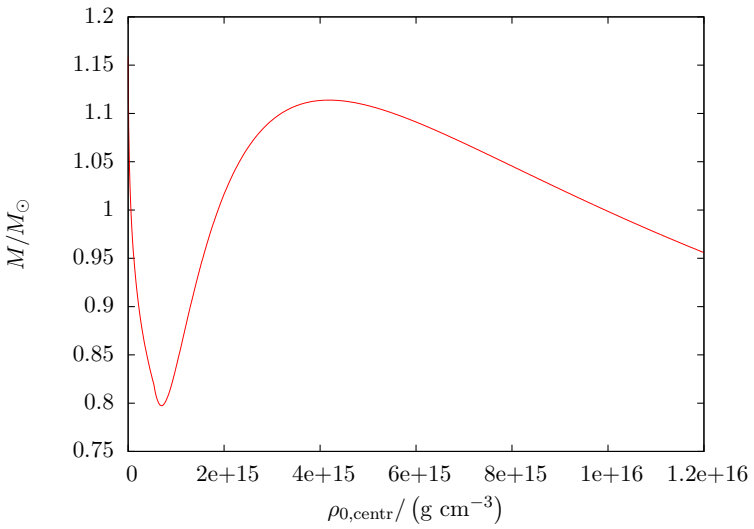

Figure 26: Total gravitational mass vs. central density for equilibrium models with a mixed equation of state with $\gamma_1 = 4/3$, $\gamma_2 = 2$, $K_2 = 100$ km^2, and $\rho_{0,\mathrm{crit}} = 5.4 \times 10^{14}$ g cm^{-3}.

Starting with a radially unstable model on the low-density branch of Figure 26 results in a collapse which is obstructed when the model passes the stable branch between the local minimum and the local maximum in Figure 26. The star then oscillates around the equilibrium position on this stable branch. Figure 27 shows an example for the worldlines describing such an obstructed collapse. Due to the lack of dissipative effects, there is no damping of the oscillation around the equilibrium configuration seen in the top half of Figure 27.

6.2.1 Electromagnetic Radiation

The oscillation around the newly formed stable stellar configuration leads to a periodical enhancement and weakening of the magnetic field in the interior of the star which influences the field in the exterior via the junction conditions at the stellar surface. This produces an electromagnetic wave travelling from the stellar surface outward. Since different models, such as with different critical densities $\rho_{0,\mathrm{crit}}$ or with different initial central densities $\rho_{0,\mathrm{centr}}$, lead to different oscillation frequencies of the newly formed neutron star, the frequency of the emerging wave will also depend on these parameters.

Figure 28 shows the dependence of the frequency of the emitted electromagnetic wave on the two parameters $\rho_{0,\mathrm{crit}}$ and $\rho_{0,\mathrm{centr}}$. The extension of the sequences of models is limited by stability beyond the local minimum in the M-R-plot (cf. Figure 26) on the high-density side and by the direct collapse to a black hole on the low-density side.

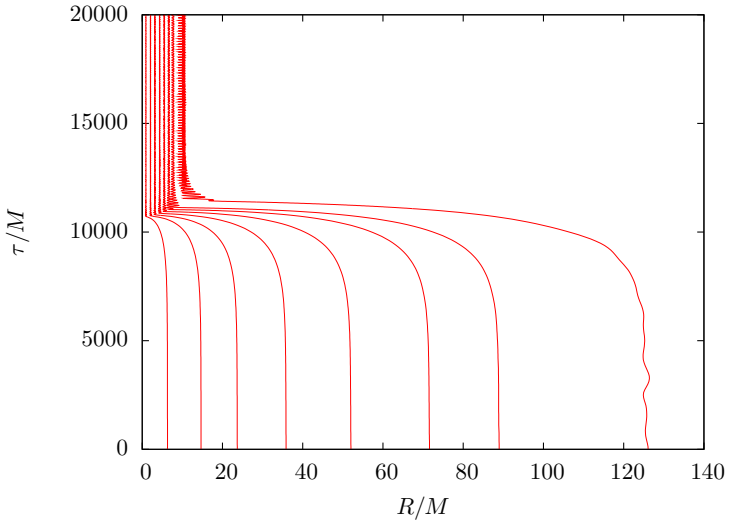

Figure 27: Worldlines of several mass-shells for the collapse of a star with a mixed equation of state with $\gamma_1 = 4/3$, $\gamma_2 = 2$, $K_2 = 100$ km^2, $\rho_{0,\mathrm{crit}} = 5.4 \times 10^{14}$ g cm^{-3}, and an initial central density of $\rho_{0,\mathrm{centr}} = 6.7 \times 10^{12}$ g cm^{-3}. The outermost mass-shell that is shown corresponds to the stellar surface.

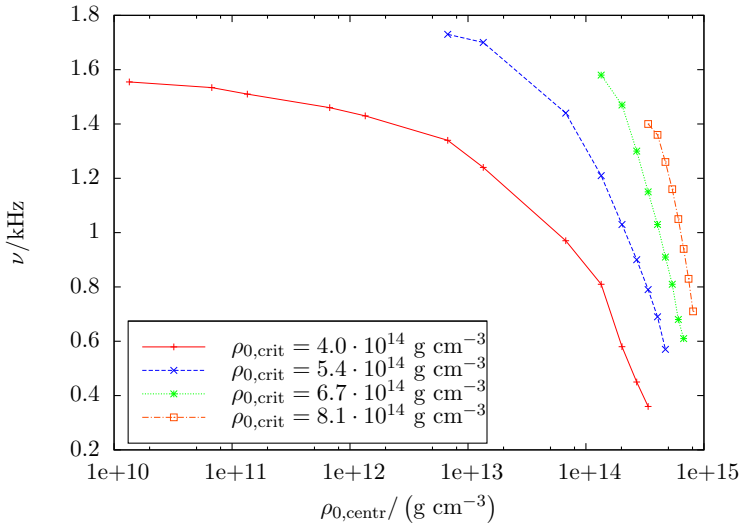

Figure 28: Frequencies of the emerging electromagnetic wave after the collapse to a neutron star, as measured at a circumferential radius of $R = 200M$, against the initial central density $\rho_{0,\mathrm{centr}}$. The solid line corresponds to a critical density of $\rho_{0,\mathrm{crit}} = 4.0 \times 10^{14}$ g cm^{-3}, the dashed line to $\rho_{0,\mathrm{crit}} = 5.4 \times 10^{14}$ g cm^{-3}, the dotted line to $\rho_{0,\mathrm{crit}} = 6.7 \times 10^{14}$ g cm^{-3}, and the dash-dotted line to $\rho_{0,\mathrm{crit}} = 8.1 \times 10^{14}$ g cm^{-3}. In all cases $\gamma_1 = 4/3$, $\gamma_2 = 2$, and $K_2 = 100$ km^2.

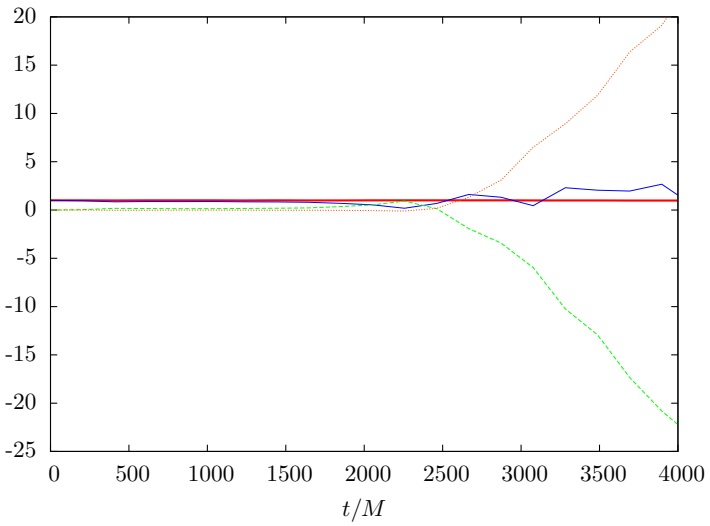

Figure 29: Energy balance of the 3-volume bounded by $R_1 = 2R_{0,\mathrm{surf}}$ and $R_2 = 300M$ for the collapse of a star with a mixed equation of state with $\gamma_1 = 4/3$, $\gamma_2 = 2$, $K_2 = 100$ km^2, $\rho_{0,\mathrm{crit}} = 5.4 \times 10^{14}$ g cm^{-3}, and an initial central density of $\rho_{0,\mathrm{centr}} = 6.7 \times 10^{12}$ g cm^{-3}. The solid line depicts the normalized energy $\mathcal{E}(t)/\mathcal{E}(t=0)$ contained within the volume, the dashed line the normalized integrated energy flux across the inner boundary $-\mathcal{I}(R_1)/\mathcal{E}(t=0)$, the dotted line the normalized integrated energy flux across the outer boundary $\mathcal{I}(R_2)/\mathcal{E}(t=0)$, and the thick line the quantity $\bar{\mathcal{E}}(t)$ defined in the text.

On the other hand, as in section 5.6.3, one can check the balance of electromagnetic energy in a given volume in the stellar exterior. Figure 29 shows the energy balance of the region bounded by $R_1 = 2R_{0,\mathrm{surf}}$ and $R_2 = 300M$. The notation is the same as in section 5.6.3. Again, the condition for the conservation of energy, equation (5.99), is satisfied with an accuracy better than two percent. This becomes manifest in the constancy of the thick curve in Figure 29. The right half of the plot shows the dashed curve declining and the dotted curve rising at roughly constant rate. This corresponds to the electromagnetic wave running into the volume under consideration at the inner boundary R_1 and out of it at the outer boundary R_2.

Instead of the time-integrated energy flux depicted by the dashed and dotted curves in Figure 29, given by equation (5.98), one can consider the energy flux across a spherical shell, i.e. the luminosity

$$L = \frac{2}{3}\left((a_{,v})^2 - (a_{,u})^2\right). \tag{6.5}$$

From this, one obtains the energy flux density, i.e. the absolute value of the Poynting vector, by dividing by the surface area of a spherical shell

$$S(R) = \frac{1}{6\pi R^2}\left((a_{,v})^2 - (a_{,u})^2\right). \tag{6.6}$$

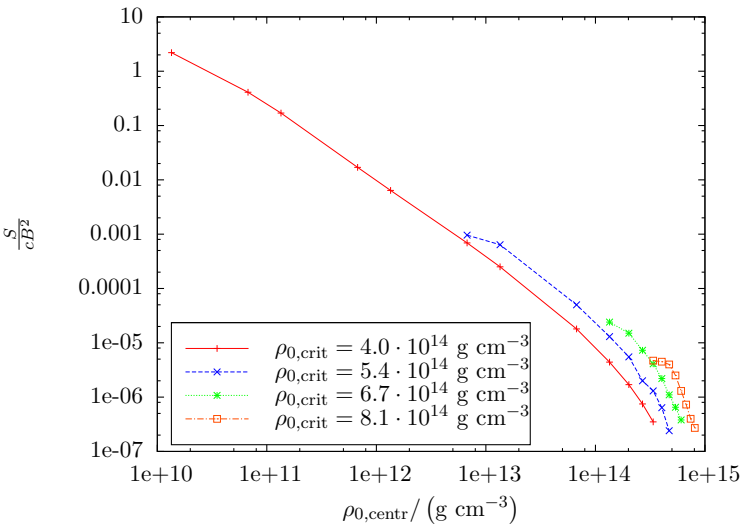

Figure 30: Ratio of the energy flux density of the emerging electromagnetic wave over the initial field strength squared, S/B^2, after the collapse to a neutron star, as measured at a circumferential radius of $R = 200M$, against the initial central density $\rho_{0,\mathrm{centr}}$. The solid line corresponds to a critical density of $\rho_{0,\mathrm{crit}} = 4.0 \times 10^{14}$ g cm^{-3}, the dashed line to $\rho_{0,\mathrm{crit}} = 5.4 \times 10^{14}$ g cm^{-3}, the dotted line to $\rho_{0,\mathrm{crit}} = 6.7 \times 10^{14}$ g cm^{-3} and the dash-dotted line to $\rho_{0,\mathrm{crit}} = 8.1 \times 10^{14}$ g cm^{-3}. In all cases $\gamma_1 = 4/3$, $\gamma_2 = 2$, and $K_2 = 100$ km^2.

Since the field a is proportional to the factor B which is a measure for the initial magnetic field strength (cf. section 5.3), the Poynting vector will be related to this factor according to

$$S \sim B^2. \tag{6.7}$$

Therefore, the quantity S/B^2, which is independent of the initial field strength, was calculated for different models. Figure 30 shows its dependence onto the critical density $\rho_{0,\mathrm{crit}}$ and the initial central density $\rho_{0,\mathrm{centr}}$.

Figure 31 is a combination of Figure 28 and 30, which shows the relation of the energy flux density to the frequency of the emerging electromagnetic wave for the four different sequences of models. From these results, we find that if one would observe the energy flux density and the frequency of the electromagnetic radiation, one could determine the critical density $\rho_{0,\mathrm{crit}}$ from Figure 31 and then determine the initial central density $\rho_{0,\mathrm{centr}}$ either from Figure 28 or 30, using the frequency or the energy flux density respectively. So the parameters of the equation of state within this model could be determined via observations.

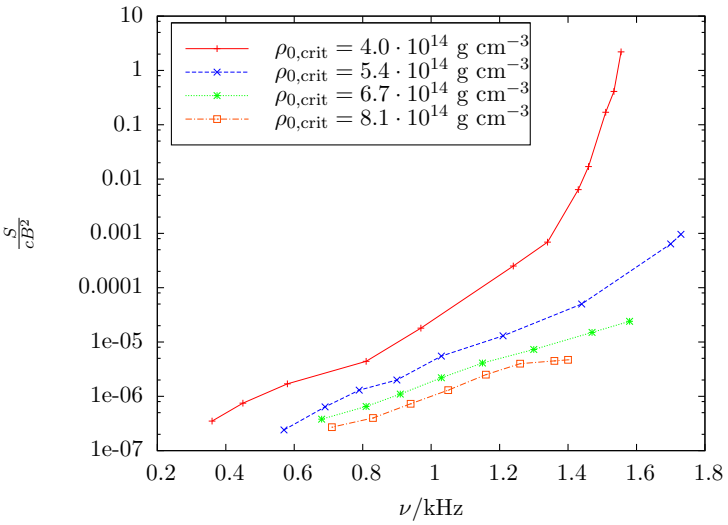

Figure 31: Ratio of the energy flux density of the emerging electromagnetic wave over the initial field strength squared, S/B^2, after the collapse to a neutron star versus its frequency, as measured at a circumferential radius of $R = 200M$. The solid line corresponds to a critical density of $\rho_{0,\mathrm{crit}} = 4.0 \times 10^{14}$ g cm^{-3}, the dashed line to $\rho_{0,\mathrm{crit}} = 5.4 \times 10^{14}$ g cm^{-3}, the dotted line to $\rho_{0,\mathrm{crit}} = 6.7 \times 10^{14}$ g cm^{-3} and the dash-dotted line to $\rho_{0,\mathrm{crit}} = 8.1 \times 10^{14}$ g cm^{-3}. In all cases $\gamma_1 = 4/3$, $\gamma_2 = 2$, and $K_2 = 100$ km^2.

7 Concluding Remarks

The results obtained with the code developed within this work are generally satisfactory. The testbed calculations performed for the case of pressureless collapse in chapter 4 are in excellent agreement with the analytical predictions. Also in the case of a collapsing polytrope, the numerical scheme is in agreement with both the theoretical predictions and the results obtained by Baumgarte, Shapiro, and Teukolsky [4]. Furthermore, we checked that the marginally stable model coincides with the model producing the maximum mass, the frequencies of oscillations of stable models are the ones predicted by Kokkotas and Ruoff [12], and that the code is stable on a large time-scale.

The electromagnetic evolution yields the expected results that are similar to the results that Baumgarte and Shapiro obtained for the case of a collapsing magnetized dust-ball [2]. Furthermore, the wavelength of the emerging radiation agrees with the one predicted by Ferrari and Mashhoon [6], the late-time fall-off of the field strength follows the t^{-4}-behavior predicted by Price [19], and the energy conservation condition is also satisfied.

Finally, the extended code that can deal with a hybrid equation of state produces models that mimic the collapse of a stellar core to a neutron star. The electromagnetic wave that emerges after the collapse carries information about the oscillations of the newly formed neutron star and therefore about the equation of state of the stellar matter. The scheme to determine the parameters of the equation of state from the properties of the radiation devised at the end of chapter 6 is a first step to link the theoretical models to potential observations.

Comparison with actual observations, however, would necessitate a more detailed and realistic description of the core-collapse scenario. Observations of the emerging electromagnetic radiation after a core-collapse supernova, for example, would be made outside of the material enveloping the core and one would have to consider the effects such as absorption that would change the properties of the radiation as it passes this material. Furthermore, a detailed consideration of the shock-front would be desirable for a more realistic description of the collapse to a neutron star.

All in all, the present code leaves a great room for generalisations that would be needed for the description of more realistic scenarios. For example, for a correct description of the likely rotation of the progenitor star, the current spherical symmetry would have to be dropped in favor of axial symmetry. Even more realistic models might be totally asymmetric, calling for a fully (3+1)-dimensional calculation instead of the current (1+1)-dimensional one. Taking into account the backractions of the electromagnetic field would be another step in the direction of a more realistic description. Considering the full backreaction would necessarily mean dropping the assumption of spherical symmetry in the equations of hydrodynamics. Finally, the polytropic equation of state could be replaced by a more realistic one and some microphysical effects could be considered.

In conclusion, the current code works with a concise model that contains the main effects and gives accurate results, but neglects many details that might become important once the predictions are linked to observations.

A Finite Difference Equations for the Hydrodynamic Evolution Scheme

In the following list of finite differnce equations used in the numerical evolution scheme, the index n denotes the position of the gridpoint with respect to the null coordinate u and the index i denotes its position with respect to the spacial coordinate A, where $i = 0$ corresponds to the stellar center and $i = I$ to the stellar surface. The equations are given in the order in which they are used in the code.

- updating U (equation (4.47)):

$$\begin{aligned} U_I^{n+1/2} &= U_I^{n-1/2} + \Delta u^n \left(e^{\psi}\right)_I^n \left(\frac{8\pi\Gamma_I^n \left(R_I^n\right)^2}{h_{I-1/2}^n} \frac{P_{I-1/2}^n + Q_{I-1/2}^n}{A_I - A_{I-1}} \right. \\ &\quad \left. - \frac{m_I^n}{\left(R_I^n\right)^2} - 4\pi R_I^n \left(P_{I-1/2}^n + Q_{I-1/2}^n\right) \right), \end{aligned} \tag{A.1}$$

$$V_i = \left(U_i^{n-1/2} - U_{i-1}^{n-1/2}\right)\left(U_{i+1}^{n-1/2} - U_i^{n-1/2}\right), \tag{A.2}$$

$$V_0 = 0, \tag{A.3}$$

$$\Delta_i = \begin{cases} 2\frac{V_i}{U_{i+1}^{n-1/2} - U_{i-1}^{n-1/2}} & \text{if } V_i \geq 0 \\ 0 & \text{otherwise} \end{cases}, \tag{A.4}$$

$$\begin{aligned} U_i^{n+1/2} &= U_i^{n-1/2} - \Delta u^n \frac{\left(e^{\psi}\right)_i^n}{1 - \left(\left(v_s\right)_i^n\right)^2} \\ &\quad \times \left\{ \left(\frac{8\pi\Gamma_i^n \left(R_i^n\right)^2}{h_i^n} \frac{P_{i+1/2}^n + Q_{i+1/2}^n - P_{i-1/2}^n - Q_{i-1/2}^n}{A_{i+1} - A_{i-1}} \right. \right. \\ &\quad \left. + \frac{m_i^n}{\left(R_i^n\right)^2} + 4\pi R_i^n \left(P_i^n + Q_i^n\right) \right) \\ &\quad + \left(\left(v_s\right)_i^n\right)^2 \left[\frac{4\pi \left(\rho_0\right)_i^n \left(R_i^n\right)^2}{A_i - A_{i-1}} \left(U_i^n - U_{i-1}^n \right. \right. \\ &\quad \left. + \frac{1}{2} \left(1 - \frac{4\pi \left(e^{\psi}\right)_i^n \left(\left(v_s\right)_i^n\right)^2 \left(\rho_0\right)_i^n \left(R_i^n\right)^2}{1 - \left(\left(v_s\right)_i^n\right)^2} \frac{\Delta u^n}{A_i - A_{i-1}} \right) \\ &\quad \left. \left. (\Delta_i - \Delta_{i-1}) \right) + \frac{2U_i^n \Gamma_i^n}{R_i^n} \right] \Bigg\} \\ &\quad + \frac{\Delta u^n}{1 - \left(\left(v_s\right)_i^n\right)^2} \frac{\Gamma_i^n}{h_i^n \left(\rho_0\right)_i^n} \frac{Q_i^n - Q_i^{n-1}}{\Delta u^{n-1/2}}, \end{aligned} \tag{A.5}$$

$$U_0^{n+1/2} = 0; \tag{A.6}$$

- extrapolating U:

$$U_i^{n+1} = U_i^{n+1/2} + \left(U_i^{n+1/2} - U_i^{n-1/2}\right) \frac{\Delta u^{n+1/2}}{2\Delta u^n}; \tag{A.7}$$

- extrapolating e^ψ:

$$\left(e^\psi\right)_i^{n+1/2} = \left(e^\psi\right)_i^n + \left(\left(e^\psi\right)_i^n - \left(e^\psi\right)_i^{n-1}\right) \frac{\Delta u^n}{2\Delta u^{n-1/2}}; \tag{A.8}$$

- updating R (equation (4.40)):

$$R_i^{n+1} = R_i^n + \Delta u^{n+1/2} \left(e^\psi\right)_i^{n+1/2} U_i^{n+1/2}; \tag{A.9}$$

- updating m temporarily (equation (4.48)):

$$m_0^{n+1} = 0, \tag{A.10}$$

$$\begin{aligned} m_i^{n+1} &= m_i^n - 4\pi\Delta u^{n+1/2} \left(e^\psi\right)_i^{n+1/2} \left(\frac{R_i^n + R_i^{n+1}}{2}\right)^2 \\ &\quad \times \left(P_i^n + Q_i^n\right) U_i^{n+1/2}; \end{aligned} \tag{A.11}$$

- updating Γ (equation (4.50)):

$$\Gamma_0^{n+1} = 1, \tag{A.12}$$

$$\Gamma_i^{n+1} = \left(1 + \left(U_i^{n+1}\right)^2 - \frac{2m_i^{n+1}}{R_i^{n+1}}\right)^{1/2}; \tag{A.13}$$

- updating ρ_0 (equation (4.51)):

$$(\rho_0)_{i+1/2}^{n+1} = \frac{3}{4\pi} \frac{\Gamma_{i+1/2}^{n+1} + U_{i+1/2}^{n+1}}{\left(R_{i+1}^{n+1}\right)^3 - \left(R_i^{n+1}\right)^3} \left(A_{i+1} - A_i\right); \tag{A.14}$$

- updating Q (equation (4.63)):

$$Q_{i+1/2}^{n+1} = \begin{cases} \kappa_1 \left(\rho_0\right)_{i+1/2}^{n+1} \left(1 + \kappa_2 \epsilon_{i+1/2}^n\right) & \text{if } U_{i+1}^{n+1} - U_i^{n+1} < 0 \\ \quad \times \left(U_{i+1}^{n+1} - U_i^{n+1}\right)^2 & \\ 0 & \text{otherwise} \end{cases}; \tag{A.15}$$

- updating P (equation (4.120)):

$$P_{i+1/2}^{n+1} = K \left((\rho_0)_{i+1/2}^{n+1}\right)^\gamma; \tag{A.16}$$

- updating ϵ (equation (4.125)):

$$\epsilon_{i+1/2}^{n+1} = \frac{K}{\gamma - 1} \left((\rho_0)_{i+1/2}^{n+1} \right)^{\gamma - 1}; \tag{A.17}$$

- updating h (equation (3.28)):

$$h_{i+1/2}^{n+1} = 1 + \epsilon_{i+1/2}^{n+1} + \frac{P_{i+1/2}^{n+1} + Q_{i+1/2}^{n+1}}{(\rho_0)_{i+1/2}^{n+1}}; \tag{A.18}$$

- updating v_s (equation (4.55)):

$$(v_s)_{i+1/2}^{n+1} = \left((\gamma - 1) \frac{h_{i+1/2}^{n+1} - 1}{h_{i+1/2}^{n+1}} \right)^{1/2}; \tag{A.19}$$

- updating m (equation (4.52)):

$$m_0^{n+1} = 0, \tag{A.20}$$

$$\begin{aligned} m_{i+1}^{n+1} &= m_i^{n+1} + \Bigg(\left(1 + \epsilon_{i+1/2}^{n+1} \right) \Gamma_{i+1/2}^{n+1} \\ &\quad - \frac{\left(P_{i+1/2}^{n+1} + Q_{i+1/2}^{n+1} \right) U_{i+1/2}^{n+1}}{(\rho_0)_{i+1/2}^{n+1}} \Bigg) (A_{i+1} - A_i); \end{aligned} \tag{A.21}$$

- updating τ (equation (4.37)):

$$\tau_i^{n+1} = \tau_i^n + \left(e^{\psi} \right)_i^{n+1/2} \Delta u^{n+1/2}; \tag{A.22}$$

- updating $\left(e^{\psi} \right)$ (equation (4.49)):

$$\left(e^{\psi} \right)_I^{n+1} = \Gamma_I^{n+1} + U_I^{n+1}, \tag{A.23}$$

$$\begin{aligned} \left(e^{\psi} \right)_i^{n+1} &= \left(e^{\psi} \right)_{i+1}^{n+1} \exp \Bigg(- \frac{U_{i+1}^{n+1} - U_i^{n+1}}{\Gamma_{i+1/2}^{n+1}} \\ &\quad - \frac{m_i^{n+1}}{\left(R_i^{n+1} \right)^3} \frac{A_{i+1} - A_i}{4\pi \, (\rho_0)_{i+1/2}^{n+1} \, R_i^{n+1} \Gamma_{i+1/2}^{n+1}} \\ &\quad - \frac{P_{i+1/2}^{n+1} + Q_{i+1/2}^{n+1}}{(\rho_0)_{i+1/2}^{n+1} \, \Gamma_{i+1/2}^{n+1} R_i^{n+1}} (A_{i+1} - A_i) \Bigg), \end{aligned} \tag{A.24}$$

$$\begin{aligned}\left(e^{\psi}\right)_0^{n+1} &= \left(e^{\psi}\right)_1^{n+1} \exp\Bigg(-\frac{U_1^{n+1}-U_0^{n+1}}{\Gamma_{1/2}^{n+1}} \\ &\quad -\frac{m_1^{n+1}}{\left(R_1^{n+1}\right)^3}\frac{A_1-A_0}{4\pi\,(\rho_0)_{1/2}^{n+1}\,R_{1/2}^{n+1}\Gamma_{1/2}^{n+1}} \\ &\quad -\frac{P_{1/2}^{n+1}+Q_{1/2}^{n+1}}{(\rho_0)_{1/2}^{n+1}\,\Gamma_{1/2}^{n+1}R_{1/2}^{n+1}}\,(A_1-A_0)\Bigg); \end{aligned} \tag{A.25}$$

- updating Δu:

$$\Delta u^{n+3/2} = \min\begin{cases} 0.9\frac{1-(v_s)_{i+1/2}^{n+1}}{(v_s)_{i+1/2}^{n+1}}\frac{R_{i+1}^{n+1}-R_i^{n+1}}{\left(U_{i+1/2}^{n+1}+\Gamma_{i+1/2}^{n+1}\right)\left(e^{\psi}\right)_{i+1/2}^{n+1}} \\ 0.02\frac{(\rho_0)_{i+1/2}^{n+1}\Delta u^{n+1/2}}{\left|(\rho_0)_{i+1/2}^{n+1}-(\rho_0)_{i+1/2}^{n}\right|} \\ 0.005\frac{R_i^{n+1}}{\left|\left(e^{\psi}\right)_i^{n+1}U_i^{n+1}\right|} \\ 0.1\frac{R_i^{n+1}-2m_i^{n+1}}{\left|\left(e^{\psi}\right)_i^{n+1}U_i^{n+1}\right|} \end{cases}, \tag{A.26}$$

where the minimum over all gridpoints is taken.

References

[1] R. Arnowitt, S. Deser, and C. W. Misner. The Dynamics of General Relativity. In L. Witten, editor, *Gravitation: An Introduction to Current Research*, chapter 7, pages 227–264. Wiley, New York, 1962.

[2] T. W. Baumgarte and S. L. Shapiro. Collapse of a Magnetized Star to a Black Hole. *Astrophysical Journal*, 585:930–947, 2003.

[3] T. W. Baumgarte and S. L. Shapiro. General-Relativistic MHD for the Numerical Construction of Dynamical Spacetimes. *Astrophysical Journal*, 585:921–929, 2003.

[4] T. W. Baumgarte, S. L. Shapiro, and S. A. Teukolsky. Computing Supernova Collapse to Neutron Stars and Black Holes. *Astrophysical Journal*, 443:717–734, 1995.

[5] G. F. R. Ellis. Relativistic Cosmology. In E. Schatzman, editor, *Cargèse Lectures in Physics*, volume 6, page 1. Gordon and Breach, New York, 1973.

[6] V. Ferrari and B. Mashhoon. New Approach to the Quasinormal Modes of a Black Hole. *Phys. Rev. D*, 30(2):295–304, 1984.

[7] J. A. Font. Numerical Hydrodynamics and Magnetohydrodynamics in General Relativity. *Living Reviews in Relativity*, 11(7), 2008.

[8] C. L. Fryer and K. C. B. New. Gravitational Waves from Gravitational Collapse. *Living Reviews in Relativity*, 6(2), 2003.

[9] T. Harada, H. Iguchi, and M. Shibata. Computing Gravitational Waves from Slightly Nonspherical Stellar Collapse to a Black Hole: Odd-parity Perturbation. *Phys. Rev. D*, 68(2):024002, 2003.

[10] J. F. Hawley, L. L. Smarr, and J. R. Wilson. A Numerical Study of Nonspherical Black Hole Accretion II – Finite Differencing and Code Calibration. *Astrophysical Journal Suppl. Ser.*, 55:211–246, 1984.

[11] W. C. Hernandez Jr and C. W. Misner. Observer Time as a Coordinate in Relativistic Spherical Hydrodynamics. *Astrophysical Journal*, 143:452–464, 1966.

[12] K. D. Kokkotas and J. Ruoff. Radial Oscillations of Relativistic Stars. *Astronomy and Astrophysics*, 366:565–572, 2001.

[13] L. D. Landau and L. M. Lifšic. *Lehrbuch der Theoretischen Physik*, volume 2: Klassische Feldtheorie. Akademie Verlag, Berlin, 1962.

[14] M. M. May and R. H. White. Hydrodynamic Calculations of General-Relativistic Collapse. *Phys. Rev.*, 141:1232–1241, 1966.

[15] M. M. May and R. H. White. Stellar dynamics and gravitational collapse. *Methods Comput. Phys.*, 7:219–258, 1967.

[16] C. W. Misner and D. H. Sharp. Relativistic Equations for Adiabatic, Spherically Symmetric Gravitational Collapse. *Phys. Rev.*, 136:B571–B576, 1964.

[17] C. W. Misner, K. S. Thorne, and J. A. Wheeler. *Gravitation.* W. H. Freeman and Company, New York, 1973.

[18] C. D. Ott. The Gravitational Wave Signature of Core-Collapse Supernovae. *Class. Quant. Grav.*, 26:063001, 2009.

[19] R. H. Price. Nonspherical Perturbations of Relativistic Gravitational Collapse I – Scalar and Gravitational Perturbations. *Physical Review D*, 5(10):2419–2438, 1972.

[20] A. D. Rendall. *Partial Differential Equations in General Relativity.* Oxford graduate texts in mathematics ; 16. Oxford University Press, Oxford, 2008.

[21] R. D. Richtmyer and K. W. Morton. *Difference Methods for Initial Value Problems.* Wiley, New York, 1967.

[22] S. L. Shapiro and S. A. Teukolsky. *Black Holes, White Dwarfs and Neutron Stars: The Physics of Compact Objects.* Wiley, New York, 1983.

[23] H. Sotani, S. Yoshida, and K. D. Kokkotas. Gravitational Radiation from Collapsing Magnetized Dust. *Phys. Rev.*, D75:084015, 2007.

[24] I. Wasserman and S. L. Shapiro. Masses, Radii and Magnetic Fields of Pulsating X-ray Sources – Is the 'Standard' Model Self-consistent. *Astrophysical Journal*, 265:1036–1046, 1983.

[25] J. R. Wilson. Numerical Study of Fluid Flow in a Kerr Space. *Astrophysical Journal*, 173:431–438, 1972.

[26] X.-H. Zhang. 3+1 Formulation of General-Relativistic Perfect Magnetohydrodynamics. *Phys. Rev. D*, 39(10):2933–2942, 1989.